A Novel Spectral Index for Vegetation Destruction Event Detection Based on Multispectral Remote Sensing Imagery

Chuanwu Zhao, *Graduate Student Member, IEEE*, Yaozhong Pan, Hanyi Wu, *Graduate Student Member, IEEE*, Shoujia Ren, *Graduate Student Member, IEEE*, Gelilan Ma, Yuan Gao, *Graduate Student Member, IEEE*, Yu Zhu, and Guifei Jing

***Abstract*—Monitoring frequent vegetation destruction events is important for ecological conservation and environmental management. Satellite remote sensing technology is a vital tool for vegetation monitoring. Compared with the classifier-based methods, the spectral index-based methods have the advantages of fast speed and low cost. However, due to the complexity of the background environment and the spectral diversity of vegetation destruction events, there is still a lack of universal spectral indices suitable for various vegetation destruction events, and the existing spectral indices lack applicability in complex scenes. In this article, we proposed a new spectral index (called baseline-based vegetation destruction index, BVDI) using the distance from the red band to the baseline formed by the green and near-infrared bands to detect various vegetation destruction events in complex scenes. PROSAIL simulation data, various possible vegetation change scenes, and multiple vegetation destruction cases were utilized to evaluate the performance of BVDI. The results showed that BVDI was superior to the four developed indices (NDVI, EVI, NDMI, and NBR) in highlighting vegetation information while suppressing background information. In addition, BVDI showed strong robustness in cases of vegetation destruction caused by events such as wildfires, logging, insect infestations, landslides, and floods. Compared with the two data products (GLADFA and CEMS), the BVDI-based method provided more detailed spatial information. In addition, BVDI exhibited broad applicability to other multispectral sensors (Landsat-8 and Landsat-9). Therefore, BVDI is an efficient and robust spectral indicator that provides technical support for regional and even global vegetation monitoring and diagnosis.**

***Index Terms*—Baseline-based vegetation destruction index (BVDI), Landsat images, natural and human factor, Sentinel-2, vegetation destruction.**

Manuscript received 6 March 2024; revised 26 May 2024; accepted 7 June 2024. Date of publication 11 June 2024; date of current version 19 June 2024. This work was supported in part by the National Natural Science Foundation of China under Grant 42192580 and Grant 42192581, and in part by the Science and Technology Program of Yunnan Province, China under Grant 202102AE090051. *(Corresponding author: Yaozhong Pan.)*

Chuanwu Zhao, Yaozhong Pan, Hanyi Wu, Shoujia Ren, Gelilan Ma, Yuan Gao, and Yu Zhu are with the State Key Laboratory of Remote Sensing Science, Faculty of Geographical Science, Beijing Normal University, Beijing 100875, China (e-mail: pyz@bnu.edu.cn).

Guifei Jing is with the Yunnan Innovation Institute of Beihang University, Kunming 650233, China.

This article has supplementary downloadable material available at https://doi.org/10.1109/JSTARS.2024.3412737, provided by the authors.

Digital Object Identifier 10.1109/JSTARS.2024.3412737

I. Introduction

VEGETATION serves as a nexus for the exchange of carbon, water, and energy between the land and the atmosphere, offering ecosystem services such as food, fiber, and fuel [1], [2], [3]. Climate change and human activities exert dual pressures on terrestrial vegetation [4], [5]. Frequent events such as logging, wildfires, floods, and landslides exacerbated vegetation destruction [6], [7]. Vegetation destruction refers to the loss of tree vegetation, which has serious impacts on the function of ecosystems [8], [9]. According to the World Resources Institute, global forest coverage shrank by 450 million hectares over the last two decades, about 10% of the global forest coverage in 2000 [10]. Over the past 20 years, it has been estimated that the area of terrestrial vegetation loss has doubled [11]. Hence, accurate detection of vegetation destruction events is valuable for ecological valuation and environmental management [12], [13], [14].

The traditional means to obtain the range of vegetation destruction relies on time-consuming and costly field surveys [15], [16]. Remote sensing technology, due to its advantages of high frequency, large coverage area, and easy access, has emerged as an indispensable tool for earth observation [10], [15], [17]. Presently, research on vegetation destruction detection can be summarized in two groups, including single-image-based classification and multitemporal image-based change detection. Among them, the method based on a single image combines the remote sensing features of vegetation destruction events with advanced classifiers and has been widely used in various vegetation destruction events [6], [18], [19], [20], [21], [22]. Cho et al. [20] realized burned-area mapping based on PlanetScope imagery using the U-Net semantic segmentation model, with an F1 score greater than 0.88. Das et al. [23] developed a convolutional neural network model to achieve accurate detection of deforestation in the Amazon region with an IoU greater than 0.94. However, the accuracy of these methods depends on the quantity and quality of training samples, and it is difficult to generalize their clustering rules for different vegetation destruction scenarios across large areas.

To address this limitation, researchers turned to spectral index-based change detection methods, which utilize multitemporal images to detect vegetation destruction [24], [25], [26],

[27], [28], [29]. Remotely sensed vegetation indices (VIs) are widely used in disturbance ecology, such as logging, wildfires, landslides, insect infestation, and mining [30], [31], [32], [33]. Alcaras et al. [28] used Sentinel-2 imagery to develop an algorithm based on normalized burn ratio (NBR) to monitor burned areas in northeastern Italy. Based on Sentinel-2 imagery, Afira and Wijayanto [29] monitored burned areas in Rokan Hilir Regency Riau, Indonesia, using a normalized difference vegetation index (NDVI). Peereman et al. [30] used the enhanced vegetation index (EVI) based on Landsat images to detect mangrove destruction caused by tropical cyclones on a global scale. The validity of the spectral index plays a crucial role in the effectiveness of multitemporal methods for identifying vegetation destruction events.

Although the multitemporal change detection method based on the spectral index has yielded satisfactory results in specific scenarios [23], [34], [35], there are still challenges to accurately detect vegetation destruction events using existing VIs. First, due to the spectral diversity of vegetation destruction, it is difficult to find a universal and valid spectral indicator [36], [37]. Existing VIs were primarily developed for specific vegetation destruction events and failed to achieve satisfactory results when applied to different events [38]. For example, logging and landslide events remove most or even all vegetation information, exhibiting spectral characteristics similar to bare soil. Vegetation greenness-based VIs like NDVI outperforms vegetation water content-based VIs such as normalized difference moisture index (NDMI) and NBR [39], [40]. However, after wildfires, an increase in black carbon concentration of soot and ash absorbs most of the solar radiation, causing the "darkening" phenomenon. In these instances, NBR performs better than NDVI [24], [29]. Second, existing VIs often neglect background interference and can misidentify other nonrelevant target pixels. For example, rapid urban construction involving land clearing or shifts in water extent or color can be mistaken for "true change" in vegetation within short time intervals [40], [41]. To accurately detect vegetation destruction events, the effects of the background environment must be considered to reduce misclassification errors [29], [35]. Therefore, it is necessary to develop a universal spectral index that can be applied to detect vegetation destruction in various scenarios.

In the above-mentioned context, the proposed index should exhibit two main features: 1) expanding the difference between vegetation and nonvegetation land cover to highlight changes in vegetation due to different damage events, and 2) narrowing the intraclass differences between nonvegetation land cover to reduce the interference of background environmental changes. To achieve these purposes, we developed a spectral index applicable to multiple types of vegetation destruction using Sentinel-2 multispectral data. We conducted extensive global testing and validation, involving various vegetation change scenes and diverse instances of vegetation destruction, to evaluate the robustness of the proposed index. This assessment involved detailed comparisons with the four most representative VIs. Our specific objectives include the following.

1) Developing a new index (BVDI) by analyzing the spectral curves of Sentinel-2 images.
2) Evaluating the sensitivity of BVDI to vegetation change and its ability to minimize intraclass variation among nonvegetation pixels.
3) Verifying the performance of BVDI in highlighting vegetation changes and suppressing background environmental changes.
4) Evaluating the performance of BVDI through comparisons with two existing data products.
5) Testing the applicability of BVDI on other multispectral data.

II. Materials

A. Study Area

The seasonal fluctuations in vegetation can influence the effectiveness of short-interval vegetation destruction monitoring [41]. Considering the differences in vegetation phenology and type across different climatic regions, different study sites were selected to assess the performance of the BVDI to ensure its robustness. Taking into account both the representativeness of the study areas and data availability, we selected several study sites in multiple regions, including the Canada, United States, Brazil, Singapore, Pakistan, China, Australia, and Mediterranean countries such as Spain, Portugal, Tunisia, Italy, and Greece to conduct our experiments. The geographical distribution of these study areas is shown in Fig. 1.

B. Data Sources

1) Remote Sensing Data: Sentinel-2 imagery was obtained from the Copernicus Data Space Ecosystem website.[1] These images were preprocessed using the Sen2Cor plug-in (version 2.11) and Sen2Res plug-in (version 5), both provided by the European Space Agency. Furthermore, we obtained Landsat-8 and Landsat-9 imagery from the United States Geological Survey (USGS) web site[2] to evaluate the broad applicability of BVDI. The ENVI software (version 5.3) was used for preprocessing the Landsat images, including radiometric calibration and atmospheric correction.

2) Standard Spectral Curve: The ECOSTRESS spectrum library[3] is the National Aeronautics and Space Administration (NASA) and the Jet Propulsion Laboratory (JPL) collaboration projects, provides spectral reflectance data for over 2000 materials [42]. This database has found wide application in studies of vegetation, bare soil, and man-made structures [43]. We obtained standardized spectral reflectance data from the ECOSTRESS spectral library for vegetation (trees, shrubs, grasses), artificial surfaces (concrete, roof tiles, roads), bare soil (Inceptisol, Entisol), and water bodies.

3) PROSAIL Simulation Data: The PROSAIL model combined the PROSPECT and SAIL models to simulate plant canopy reflectance, linking leaf biochemical content to canopy structure [44], [45]. PROSAIL model is widely used for retrieving biophysical properties of vegetation in agriculture, forestry,

[1] [Online]. Available at: https://dataspace.copernicus.eu/.
[2] [Online]. Available at: https://earthexplorer.usgs.gov/.
[3] [Online]. Available at: https://speclib.jpl.nasa.gov/.

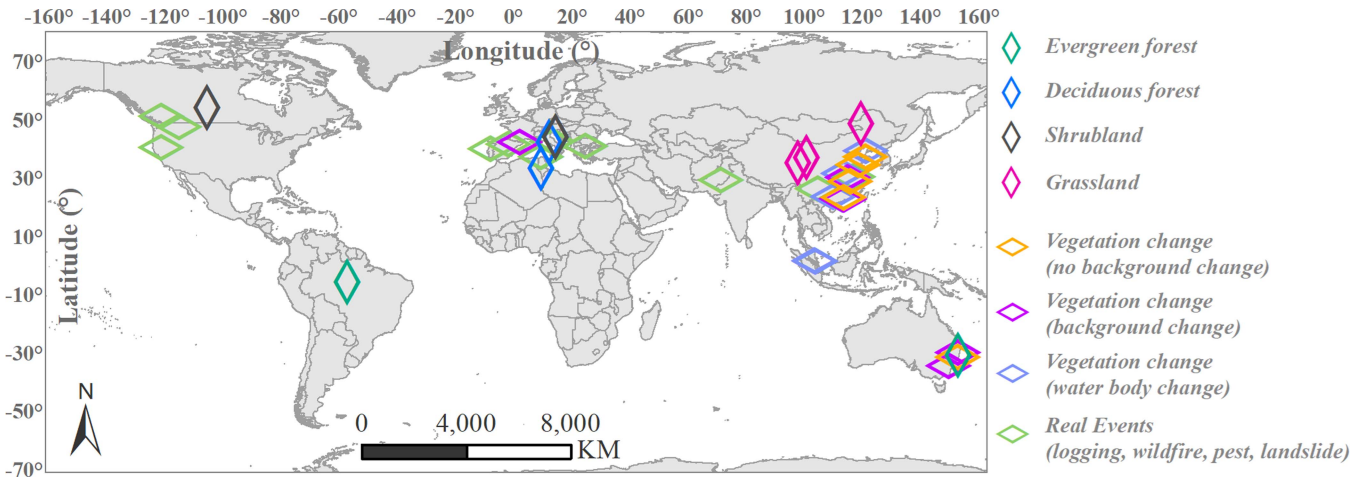

Fig. 1. Distribution of the study area.

TABLE I
PARAMETERS OF THE PROSAIL MODEL

Element	Parameter	Variable (unit)	Range of variation	Value
Leaf	Chlorophyll content	Cab (μg cm^{-2})	0–80	10, 30, 50, 70
	Structural coefficient	N (–)	1–4	1.3
	Carotenoid content	Car (μg cm^{-2})	0–20	0
	Water content	Cw (g cm^{-2})	0.004–0.04	0.012
	Brown pigment content	Cbrown (–)	0–20	8
	Dry matter content	Cm (g cm^{-2})	0.001–0.01	0.005
Canopy	Leaf area index	LAI (–)	0.1–8.1	1, 2, 3, 4, 5, 6, 7, 8
	Hot spot	hspot (–)	0.01–1	0.2
	Average leaf angle	ALA (degree)	20–70	50
	Solar zenith angle	tts (degree)	0–75	30
	View zenith angle	tto (degree)	0–75	0
	View azimuth angle	psi (degree)	0–360	0
	Soil brightness	psoil (–)	0.01–0.3	0.1
	Fraction of diffuse skylight	skyl (–)	0–1	0.1

and ecology [46], [47]. The code of PROSAIL model was acquired from the website.[4] We referred to the parameter settings of related studies [48], [49], [50] utilizing PROSAIL model, and Table I lists the detailed parameters used in this article.

4) Reference Data: The sample points used to calculate the confusion matrix were chosen by visual interpretation of Google Earth maps.[5] Sample point data for each study site were selected at a 1:1 ratio of vegetation destruction pixels to background pixels. In addition, two vegetation products, including Global Land Analysis and Discovery Forest Alerts (GLADFA) data[6] and Copernicus Emergency Management Service (CEMS) data[7] were selected for further validation. GLADFA is a global forest change product developed using Landsat imagery and updated annually with a spatial resolution of 30 m. The accuracy of forest loss detection in GLADFA data is 87.0–87.8% globally [8]. CEMS is an emergency map of European hazards (including wildfires) in vector format. Some studies have noted that CEMS data have an accuracy of over 90% for burned area monitoring [51]. Specific reference data information is provided in Table SI.

III. METHODOLOGY

As shown in Fig. 2, the workflow of this study consists of two parts: 1) construct a novel index (named BVDI) and 2) evaluate the performance of BVDI. First, Sentinel-2 and Landsat multispectral data were preprocessed. Sample points of various land cover and vegetation destruction events were selected and their spectral characteristics were analyzed to develop BVDI. Second, the dual-temporal image difference method was used to evaluate the performance of BVDI in six experiments. The evaluation method includes a detailed comparison with four representative indexes and two data products

[4][Online]. Available at: http://teledetection.ipgp.jussieu.fr/prosail/.
[5][Online]. Available at: https://earth.google.com/web/.
[6][Online]. Available at: https://glad.umd.edu/dataset.
[7][Online]. Available at: https://emergency.copernicus.eu/.

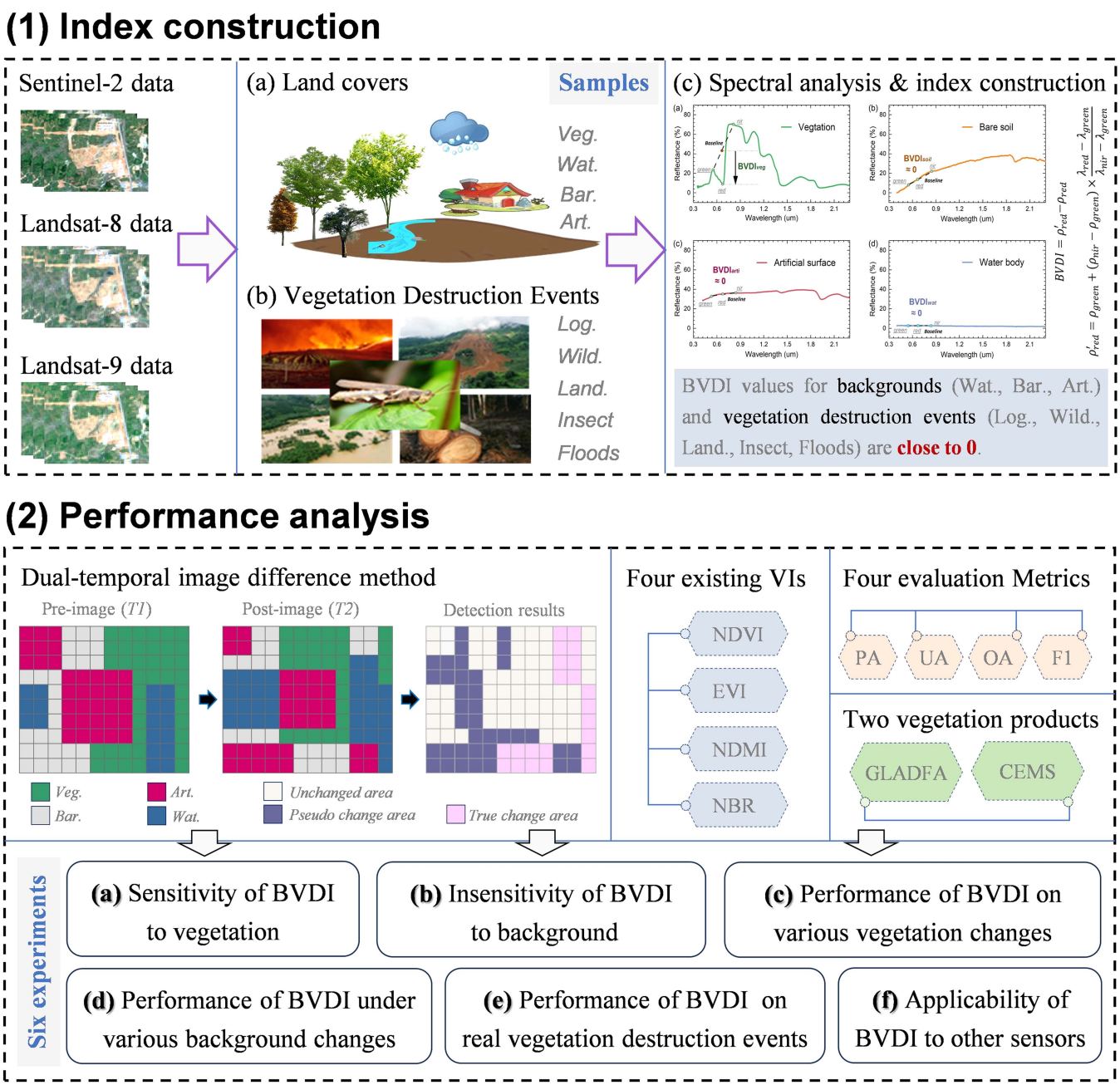

Fig. 2. Technical framework for the development and validation of the BVDI index in this study. Note that "Veg." represents vegetation, "Wat." represents water body, "Bar." represents bare soil, "Art." represents artificial surface, "Log." represents logging, "Wild." represents wildfire, and "Land." represents landslide.

and a calculation of confusion matrix for quantitative accuracy evaluation.

A. Design of BVDI

1) Spectral Analysis: Comprehensive spectral analysis is a prerequisite for the development of effective indicators. Considering the complexity of the background environment and spectral diversity of vegetation destruction events, we analyzed the spectral curves of several representative vegetation destruction events as well as several typical land covers.

Fig. 3 illustrates the spectral curves of four typical land covers. It is not difficult to see that vegetation exhibited a distinctive spectral profile. The peaks of vegetation occurred in the green band and the near infrared (NIR) band, and the troughs in the red band, which was different from the background environment (i.e., nonvegetation land cover). Artificial surfaces and bare soil exhibited similar spectral trends but different spectral values. In addition, water bodies consistently exhibited the lowest spectral reflectance in the visible-near-infrared band. Generally, in the green, red, and NIR bands, the spectral curve shape of vegetation exhibited a distinct "V-shaped valley" characteristic, whereas the spectral curve shape of nonvegetation land cover exhibited

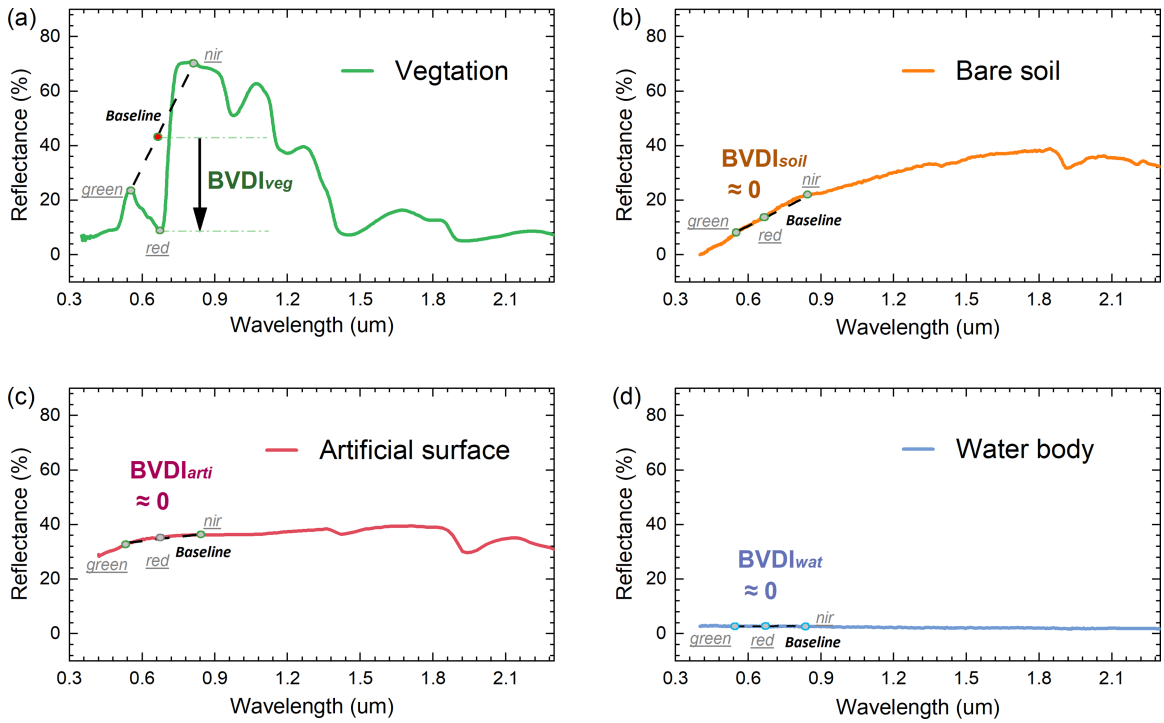

Fig. 3. Spectral profiles of typical land cover types from ECOSTRESS spectral library. (a) Spectral curves of vegetation. (b) Spectral curve of bare soil. (c) Spectral curves of artificial surface. (d) Spectral curves of water body.

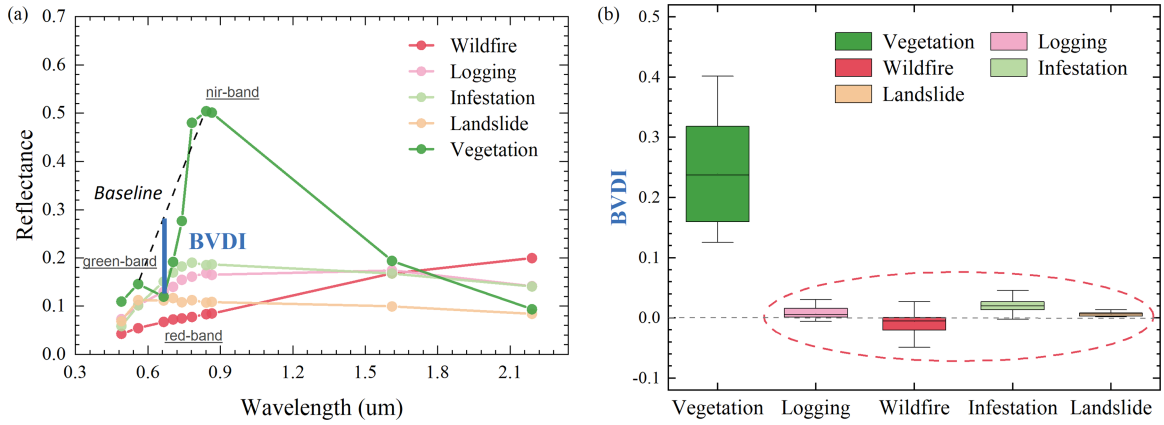

Fig. 4. (a) Spectral profiles of vegetation destruction events based on Sentinel-2 data. (b) Statistical distribution of vegetation destruction events.

a "near-linear" characteristic. This characteristic can be utilized to highlight vegetation information in the background environment.

Fig. 4 shows the spectral curves of several representative vegetation destruction events. It was easy to see that vegetation destruction events had spectral diversity, especially when wildfires had unique spectral characteristics. Spectral analysis reveals that logging, landslides and insect infestations lead to destruction of vegetation structure and reduction of chlorophyll content, presenting the spectral characteristics of bare soil. Comparatively, wildfires resulted in a charcoal-black soil background, thus absorbing more visible light and peaking in shortwave infrared (SWIR) band. Interestingly, the spectral curve shape of various vegetation destruction events also exhibited a "near-linear" signature in the green, red, and NIR bands. This property is of great value in detecting diverse vegetation destruction events.

2) Construction of BVDI: To achieve accurate detection of vegetation destruction, the proposed index must overcome the challenges posed by the spectral diversity of vegetation destruction events and the complexity of background environment. Therefore, the proposed index should exhibit target sensitivity and interference insensitivity [24], [28], [52]. In other words, 1) vegetation sensitivity: effective for vegetation changes caused by various events; and 2) nonvegetation insensitivity: insensitive to various changes in the background environment. Spectral

analysis showed that the green, red, and NIR band are helpful to detect vegetation destruction events.

Therefore, the construction principle of the BVDI can be summarized in the following three aspects.

1) Vegetation shows an obvious trough in the red band, which is conducive to highlighting vegetation information in the background environment.
2) The spectral curve shape of nonvegetation land cover (that is, the background environment) in green, red, and NIR bands exhibits a "near-linear" feature. This feature reduces the intra-class difference of nonvegetation land covers, which is essential for suppressing background environment information.
3) The spectral curve shape of various vegetation destruction events in green, red, and NIR bands exhibits a "near-linear" feature, which helps to highlight various changes in vegetation.

This is the theory behind the applicability of BVDI to the detection of various vegetation destruction events. Hence, the depth parameter of the spectral curve shape is proposed to express the above characteristics. We designed the BVDI utilizing the distance between the red band and the baseline formed by the green and NIR bands. The mathematical expression is as follows:

$$\mathrm{BVDI} = \rho'_{\mathrm{red}} - \rho_{\mathrm{red}} \tag{1}$$

$$\rho'_{\mathrm{red}} = \rho_{\mathrm{green}} + (\rho_{\mathrm{nir}} - \rho_{\mathrm{green}}) \times \frac{\lambda_{\mathrm{red}} - \lambda_{\mathrm{green}}}{\lambda_{\mathrm{nir}} - \lambda_{\mathrm{green}}} \tag{2}$$

where ρ_{green}, ρ_{red}, and ρ_{nir} represent the reflectance value of the green, red, and NIR band, respectively. λ_{green}, λ_{red}, and λ_{nir} represent the wavelength value of the green, red, and NIR bands, respectively. The BVDI values for vegetation are much greater than 0, and the BVDI values for background and vegetation destruction events are close to 0 (see Figs. 3 and 4). This is critical for accurate detection of vegetation destruction.

B. Existing VIs for Vegetation Disturbance Detection

Existing VIs used in vegetation destruction research mainly include greenness-based VIs (e.g., NDVI and EVI) and water content-based VIs (e.g., NDMI and NBR) [6], [53]. EVI effectively improved the phenomenon of vegetation saturation in NDVI [47], [54]. NDMI and NBR also have good performance in some vegetation destruction scenarios [5], [55], [56]. Therefore, the above four representative VIs were selected for detailed comparison with BVDI. These indices are calculated as follows:

$$\mathrm{NDVI} = \frac{\rho_{\mathrm{nir}} - \rho_{\mathrm{red}}}{\rho_{\mathrm{nir}} + \rho_{\mathrm{red}}} \tag{3}$$

$$\mathrm{EVI} = 2.5 \times \left(\frac{\rho_{\mathrm{nir}} - \rho_{\mathrm{red}}}{\rho_{\mathrm{nir}} + 6\rho_{\mathrm{red}} - 7.5\rho_{\mathrm{blue}} + 1} \right) \tag{4}$$

$$\mathrm{NDMI} = \frac{\rho_{\mathrm{nir}} - \rho_{\mathrm{swir1}}}{\rho_{\mathrm{nir}} + \rho_{\mathrm{swir1}}} \tag{5}$$

$$\mathrm{NBR} = \frac{\rho_{\mathrm{nir}} - \rho_{\mathrm{swir2}}}{\rho_{\mathrm{nir}} + \rho_{\mathrm{swir2}}}. \tag{6}$$

Here, ρ_{blue} and ρ_{swir} are the reflectance values of the blue and SWIR bands, respectively.

C. Dual-Temporal Image Difference Method

Image difference method (7) can intuitively reflect the level of information change, which is a simple and effective change detection scheme [57], [58], [59]. This scheme can be used to assess the ability of indicators to highlight "true change" and inhibit "pseudo change". Here, "true change" denotes the vegetation change information, and "pseudo change" denotes the nonvegetation change information, including water body, bare soil, and artificial surface change

$$\mathrm{DVI} = \mathrm{VI}_{\mathrm{Pre}} - \mathrm{VI}_{\mathrm{Post}}. \tag{7}$$

Here, $\mathrm{VI}_{\mathrm{Pre}}$ and $\mathrm{VI}_{\mathrm{Post}}$ represent the VI images before and after vegetation destruction, respectively.

D. Evaluation Metrics

All the collected sample points were used to generate the confusion matrix. The ROC curve was used to determine the optimal threshold for DVI [60], [61]. Specifically, sample points selected from high-resolution images were employed to calculate the accuracy of each index at different thresholds, which facilitates the determination of the optimal threshold. Overall accuracy (OA), producer accuracy (PA), user accuracy (UA), and F1 score were chosen to quantitatively evaluate the accuracy of the detection results [8], [60], [61].

IV. Experiments

A. Sensitivity Test of VIs to Vegetation Parameters

Using the PROSAIL model, we simulated the spectral reflectance under different leaf biochemical contents and canopy structures to evaluate the sensitivity of the BVDI to vegetation parameters, specifically chlorophyll content (Cab) and leaf area index (LAI). We found that all five VIs exhibited positive correlations with LAI, with BVDI demonstrating the highest sensitivity to LAI. NDVI exhibited an evident saturation effect; as LAI increased to four, the increase in NDVI became insignificant [see Fig. 5(a), (f), (k), and (p)]. The correlation between NDVI and LAI was lowest, with correlation coefficients (R2) of 0.76–0.83 at different Cab values. The results show that NDVI has a saturation phenomenon and asymptotic signal under high biomass conditions [62]. EVI and BVDI were highly correlated with LAI with R2 values of 0.96–0.97 and 0.97–0.98, respectively. The correlation between EVI and LAI decreased with increasing Cab values. The R2 values of NDMI and NBR with LAI were both greater than 0.85, but they were less sensitive to the change in vegetation chlorophyll content. In contrast, BVDI consistently showed a strongly linear correlation with LAI, with R2 values of 0.97–0.98. These results confirm that BVDI exhibits the highest sensitivity to vegetation change compared to the other VIs, which is crucial for vegetation change detection.

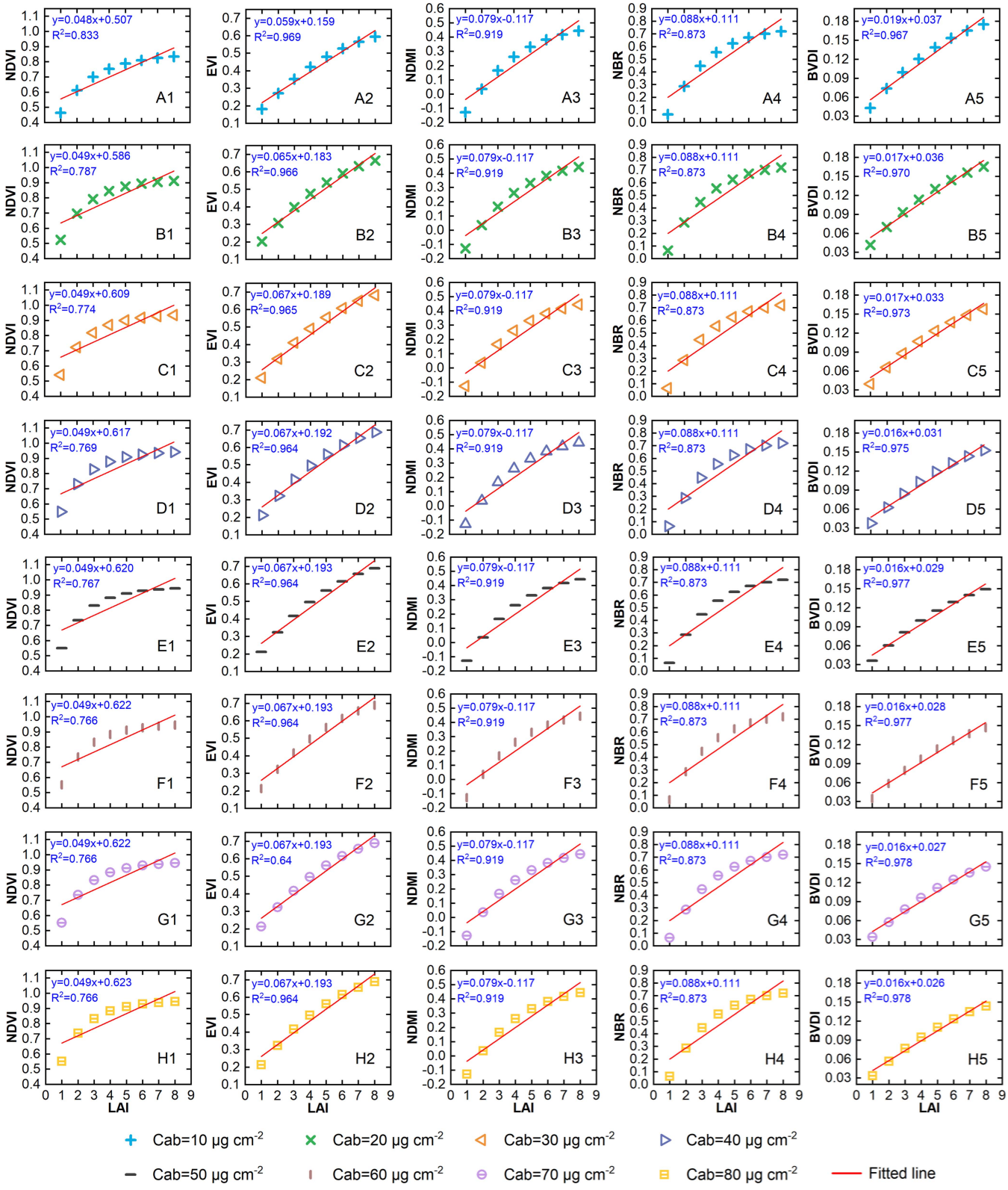

Fig. 5. Correlation of NDVI, EVI, NDMI, NBR, and BVDI with LAI for chlorophyll content at (A1-A5) 10 μg cm^{-2}, (B1-B5) 20 μg cm^{-2}, (C1-C5) 30 μg cm^{-2}, (D1-D5) 40 μg cm^{-2}, (E1-E5) 50 μg cm^{-2}, (F1-F5) 60 μg cm^{-2}, (G1-G5) 70 μg cm^{-2}, and (H1-H5) 80 μg cm^{-2}.

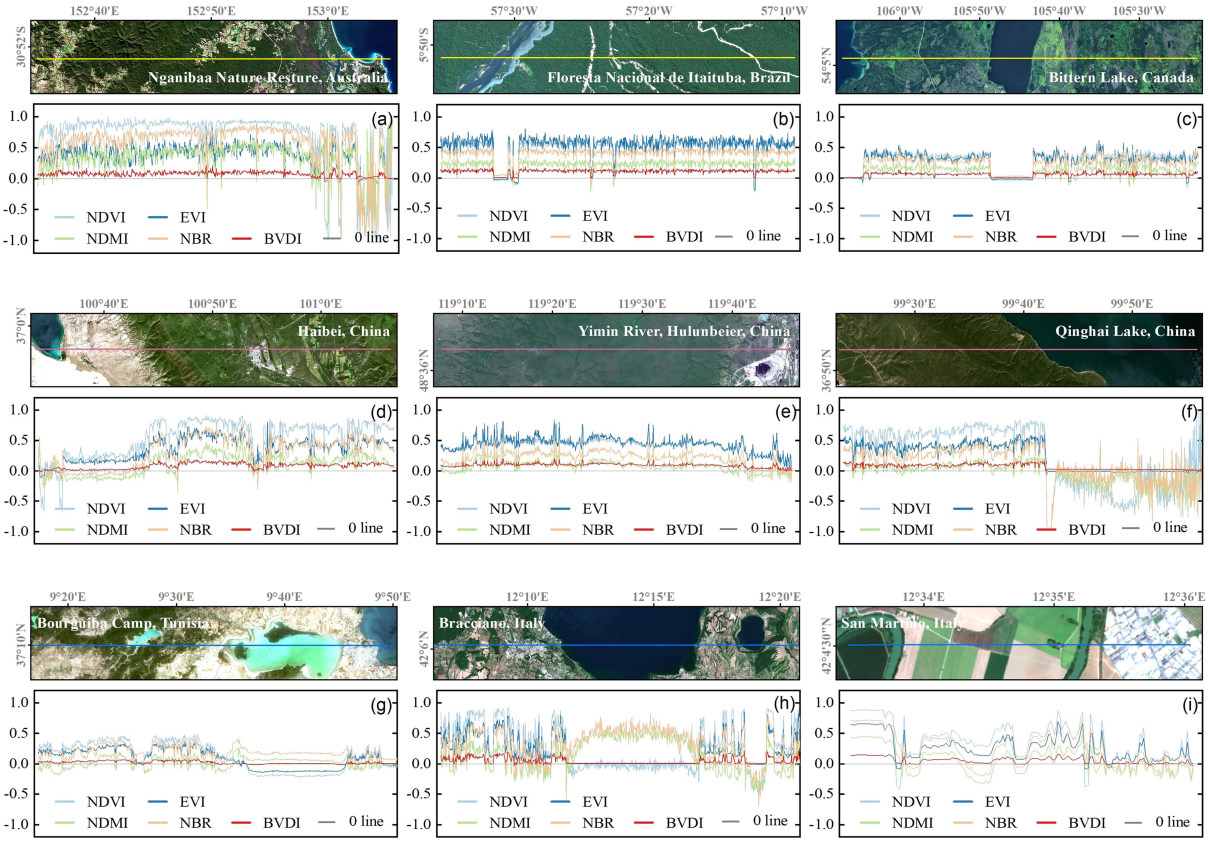

Fig. 6. Performance of VIs in (a) Australia: evergreen forest, (b) Brazil: evergreen forest, (c) Canada: shrubland, (d) China: grassland, (e) China: grassland, (f) China: grassland, (g) Tunisia: deciduous forest, (h) Italy: deciduous forest, and (i) Italy: shrubland.

B. Sensitivity Test of VIs to Background Environments

We chose study sites with different vegetation types and background environments to illustrate the effectiveness of the BVDI in highlighting vegetation while suppressing nonvegetation. As depicted in Fig. 6(a)–(c), all five VIs exhibited similar fluctuation trends across different vegetation types, including tree, shrub, and grass. Meanwhile, BVDI exhibited the highest stability ($\sim$0 value) on the water body. In sparse vegetation areas, NDVI, EVI, NDMI, and NBR demonstrated susceptibility to soil background effects [see Fig. 6(e) and (f)] and exhibited significant variability on the water body. In contrast, BVDI had the best performance in reducing intraclass differences among nonvegetation [see Fig. 6(d), (g), and (h)]. For example, there were large differences in EVI values between water bodies and bare soil [see Fig. 6(d)]. In other words, the water body, bare soil, and artificial surface exhibited similar BVDI ranges ($\sim$0 value). Furthermore, BVDI showed greater robustness on different types of water body, bare soil, and artificial surface [see Fig. 6(g)–(i)].

Subsequently, we analyzed the distribution characteristics of each index and calculated the separation (i.e., the M index) among all land covers. It is calculated as follows:

$$M = \frac{|\mu_1 - \mu_2|}{\sigma_1 + \sigma_2}. \tag{8}$$

Here, μ and σ represent the mean and standard deviation, respectively. When the M value exceeds 1, it means that the two land covers are more easily separated. It also means that the conversion between the two land covers will present a significant change value on the dual-temporal difference image.

As illustrated in Fig. 7, high values of all VIs represent vegetation information, while low values represent nonvegetation information. For all five VIs, the M-index between vegetation and nonvegetation exceeded one, indicating that all VIs can effectively highlight vegetation change information. However, NDVI, EVI, NDMI, and NBR were unable to minimize intraclass differences between nonvegetation. Specifically, on NDVI, EVI, and NDMI images, the distinction between water bodies and bare soil was substantial (M-index greater than one). On NDVI and EVI images, the M-index between bare soil and artificial surfaces was near or even greater than one. On NBR images, the M-index between the water body and artificial surfaces exceeded 0.60. This implies that changes between water bodies and bare soil, as well as between bare soil and artificial surfaces, could impact the accuracy of vegetation change detection when using NDVI, EVI, NDMI, and NBR. In contrast, on the BVDI image, the M-index between all the nonvegetation was less than one. The results confirm that BVDI exhibits greater stability on nonvegetation and remains less sensitive to nonvegetation changes. This characteristic is critical for the accurate detection of vegetation changes.

C. Performance in Various Vegetation Change Scenarios

We selected various scenarios in which vegetation changes to bare soil, artificial surface, and water body to assess the

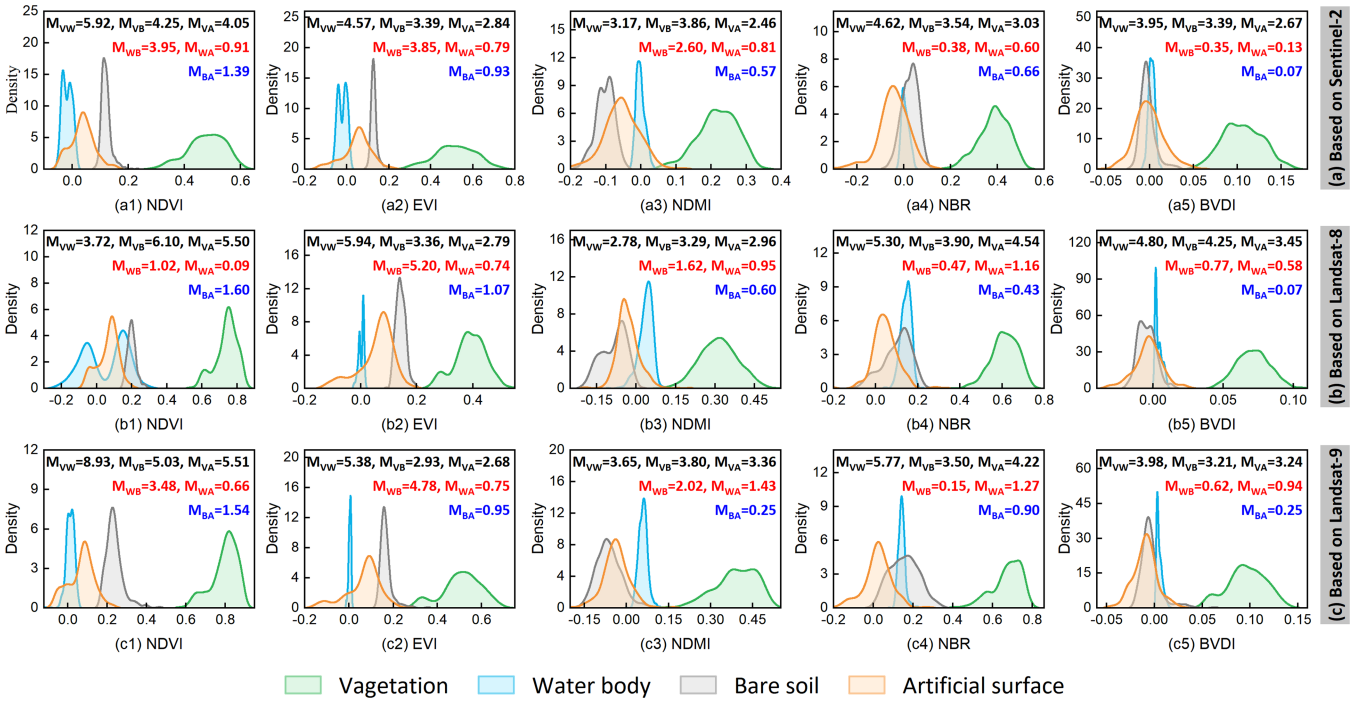

Fig. 7. Distribution of typical land covers on VIs based on (a) Sentinel-2 imagery, (b) Landsat-8 imagery, and (c) Landsat-9 imagery. M_{VW}, M_{VB}, and M_{VA} represent the separation of vegetation from water body, bare soil, and artificial surface, respectively; M_{WB} and M_{WA} represent the separation of water body from bare soil and artificial surface, respectively; M_{BA} represents the separation of bare soil and artificial surface.

performance of the BVDI. To ensure an objective comparison, we applied percentage truncation linear stretching to the DVI results. As shown in Fig. 8, BVDI had the best performance in highlighting vegetation change information in all scenarios, while NDMI and NBR had the worst results. As shown in Fig. 8(a3) and (b2), NDMI and NBR were unable to highlight changes in low-coverage vegetation, omitting numerous pixels of vegetation change. For scenes in which vegetation changes to the water body, NDVI, NDMI, and NBR were not always effective [see Fig. 8(c)]. Overall, BVDI exhibited strong robustness across different vegetation change scenes.

Fig. 9 shows the accuracy assessment of the detection results for all VIs. In all vegetation change scenarios, BVDI outperformed NDVI, EVI, NDMI, and NBR, with mean values of OA and F1 greater than 0.95. For weak vegetation changes and vegetation changes to water bodies, both NDMI and NBR did not perform well, with PA values less than 0.70, indicating that these methods have large omission errors. Furthermore, variations in light conditions had an impact on the identification results of NDVI, EVI, NDMI, and NBR. Specifically, the UA value of NDVI was 0.87 in scenario a4, and the UA values of EVI, NDMI, and NBR were less than 0.90 in scenarios b3 and b4. Overall, BVDI demonstrated its ability to effectively highlight various types of vegetation changes.

D. Performance in Background Change Scenarios

Whether the vegetation change information can be accurately detected in the context of background environmental changes provides a basis for determining the applicability of indicators in complex scenarios. In this section, various background environmental change scenarios were chosen to demonstrate the robustness of BVDI.

Fig. 10 shows the results of vegetation destruction detection in the context of bare soil and artificial surface changes. It is evident that BVDI outperformed NDVI, EVI, NDMI, and NBR in highlighting vegetation changes and suppressing changes in bare soil and artificial surfaces. NDVI was ineffective in highlighting changes in high-cover vegetation [see Fig. 10(a) and (b)] and performed poorly in low-cover vegetation areas [see Fig. 10(c)]. Similarly, NDMI and NBR failed to detect changes in low-cover vegetation effectively [see Fig. 10(c)]. EVI omitted some pixels where the vegetation becomes bare soil [see Fig. 10(d)]. In addition, NDMI and NBR misidentified the change pixels of bare soil [see Fig. 10(f)], artificial surface [see Fig. 10(i)], and water body [see Fig. 10(j)] as vegetation change information.

PA, UA, OA, and F1 values were calculated for the above-mentioned results, as shown in Fig. 11. We found that BVDI had the highest detection accuracy in all cases, with OA and F1 values greater than 0.90. For the cases in Fig. 10(a) and (b), the UA of NDVI was less than 0.85, while OA and F1 were both less than 0.90. This suggests that NDVI incorrectly labeled background change information. For the cases in Fig. 10(c), the PA for NDVI, NDMI, and NBR was less than 0.70, and the OA and F1 values were less than 0.85. For Fig. 10(d), (f), and (j), the PA for EVI was less than 0.82, indicating vegetation change information was omitted. For the cases in Fig. 10(i) and (j), the UA of NBR and NDMI was less than 0.85, indicating that they exhibited large misclassification errors. Overall, BVDI

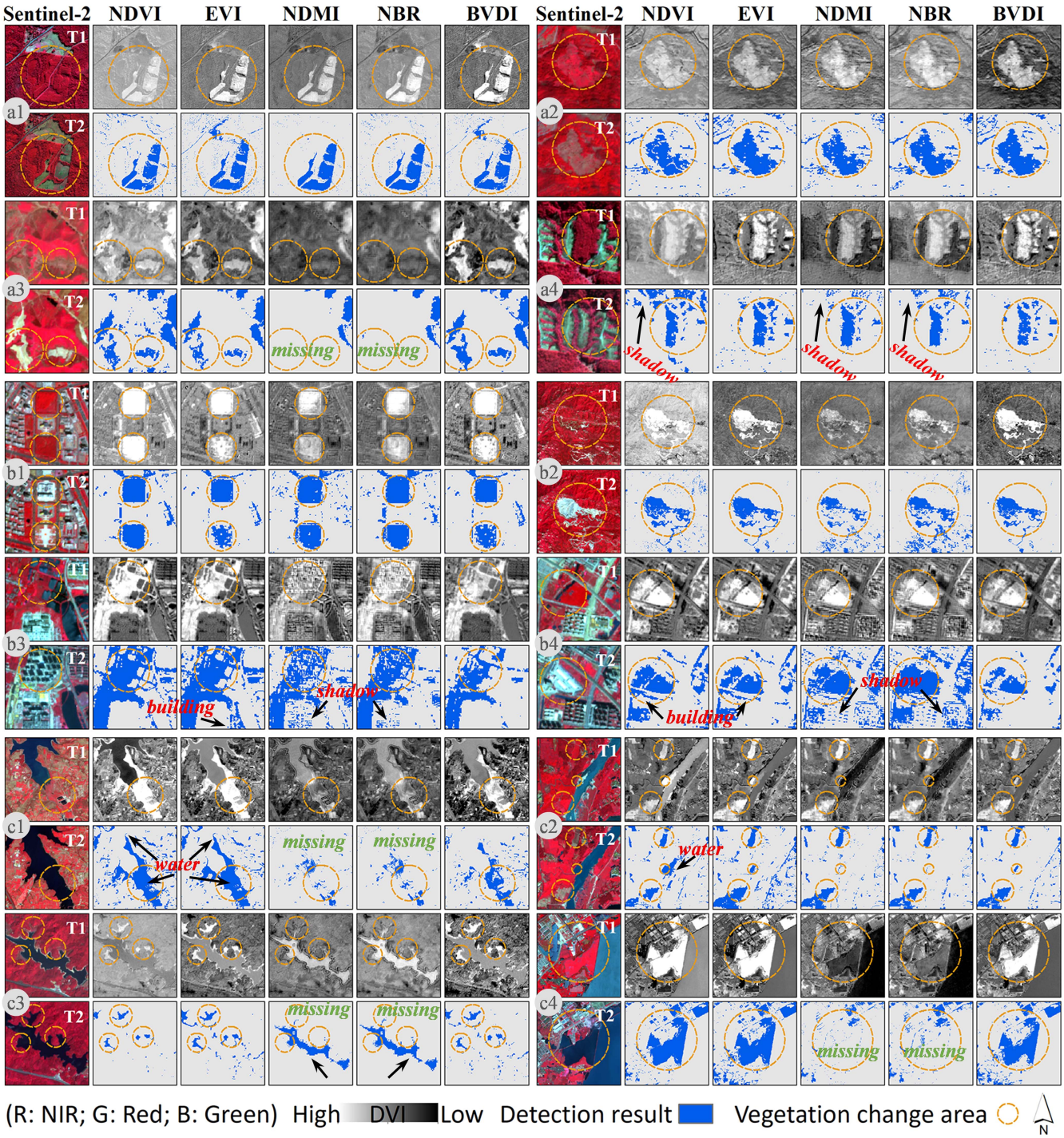

Fig. 8. Performance of VIs in different vegetation change scenes. (a1)–(a4) Vegetation changes to bare soil. (b1)–(b4) Vegetation changes to an artificial surface. (c1)–(c4) Vegetation changes to the water body. The black and white plots represent visualization results of the index difference (i.e., DVI).

performed best in highlighting changes in vegetation and suppressing changes in the background environment.

Fig. 12 shows the results of vegetation destruction detection in the context of water body changes. In general, BVDI outperformed NDVI, EVI, NDMI, and NBR in emphasizing vegetation changes and suppressing water changes. NDVI and EVI incorrectly highlighted changes from bare soil to the water body [see Fig. 12(a), (c), and (j)], labeling them as vegetation change pixels. In addition, NDVI was affected by changes in watercolor [see Fig. 12(h)]. NDMI and NBR incorrectly emphasized the changes in water body color [see Fig. 12(a), (b), (g)–(i)], misidentifying them as vegetation change pixels. Moreover, NDMI and NBR incorrectly highlighted the change from water body to bare soil [see Fig. 12(j)]. In addition, NDMI

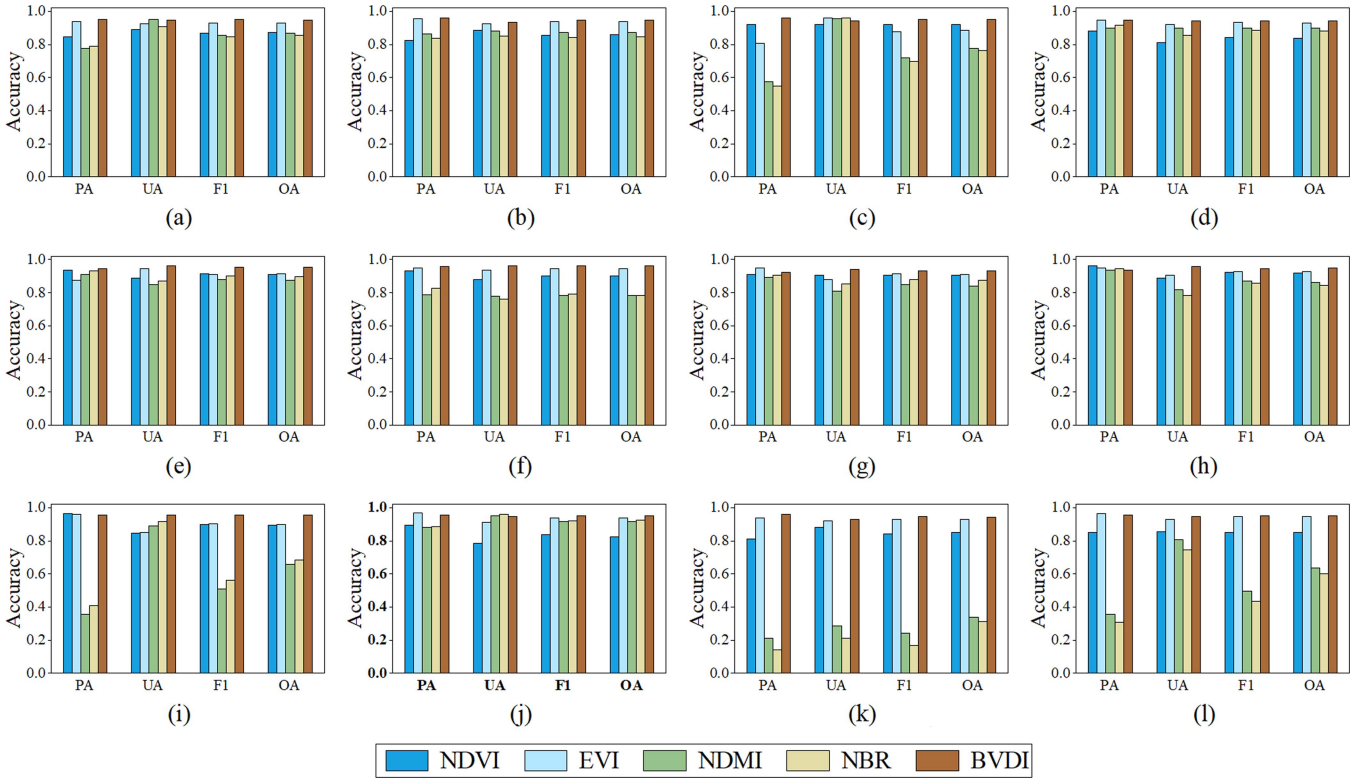

Fig. 9. Accuracy of the results of VIs under different vegetation change scenes in study sites (or Fig. 8) (a) a1, (b) a2, (c) a3, (d) a4, (e) b1, (f) b2, (g) b3, (h) b4, (i) c1, (j) c2, (k) c3, and (l) c4.

and NBR omitted a large number of pixels where vegetation changed to the water body [see Fig. 12(c) and (d)].

Fig. 13 shows the accuracy calculated for the above-mentioned detection results. Similarly, in all cases, the detection accuracy of the BVDI was higher than the other four metrics. For the cases in Fig. 12(c) and (j), the UA of EVI was less than 0.85, which indicates that it misidentified background change information. For the cases in Fig. 12(h) and (i), the UA of NDVI, NDMI, and NBR were less than 0.80, and the values of OA and F1 were less than 0.85. The experimental results revealed that the BVDI was applicable to diverse vegetation change scenes and showed robustness in complex background environments.

E. Performance in Real Vegetation Destruction Events

In the context of intense anthropogenic activity and frequent climate change, logging, insect infestations, and wildfires are common vegetation destruction events. In addition, landslides, as a geological hazard, also destroy vegetation growth, especially in mountainous areas with high-intensity precipitation. Also, floods caused by extreme rainfall can damage cultivated land, thus affecting crop growth. To further evaluate the performance of BVDI, we selected several real vegetation destruction events, including wildfire, logging, insect infestation, landslide, and flood (see Fig. 14).

We calculated the PA, UA, OA, and F1 scores of the results, as listed in Table II. It is easy to see that BVDI had the best performance in all vegetation destruction events, with OA and F1 values exceeding 0.90. Although all five VIs effectively detected vegetation changes caused by loggings, NDVI, NDMI, and NBR were susceptible to changes in water body [see Fig. 14(a) and (b)]. As shown in Fig. 14(b), NDVI, NDMI, and NBR incorrectly identified the pixels of water body change, with UA values of 0.833, 0.773, and 0.784 and OA values of 0.878, 0.832, and 0.847, respectively (see Table II). EVI omitted some low-cover vegetation change information [see Fig. 14(a)], with UA, F1, and OA values of 0.769, 0.839, and 0.823. In the case of vegetation pest events, NDMI and NBR performed poorly, missing numerous "true change" pixels [see Fig. 14(c)], with PA and OA values below 0.75. NDVI also failed to detect weak changes in high-coverage vegetation [as shown in the white box in Fig. 14(c)], with PA and OA values of 0.823 and 0.863. Although NDVI, NDMI, and NBR were able to accurately identify the extent of vegetation destruction caused by landslides and wildfires, they incorrectly labeled "pseudo-change" pixels caused by changes in water bodies [see Fig. 14(d) and (e)]. The UA values of NDVI, EVI, NDMI, and NBR were 0.690, 0.752, 0.772, and 0.784, respectively. For flood events, NDVI and EVI misidentified background information (e.g., flooded bare land) with UA of 0.862 and 0.873, respectively [see Fig. 14(g)]. NDM and NBR showed poor performance in detecting vegetation destruction caused by flood events, missing numerous vegetation change pixels, and their F1 scores and OA values were both less than 0.85. In contrast, BVDI exhibited a distinct advantage in identifying the extent of vegetation destruction and mitigating the interference of changes in the background environment,

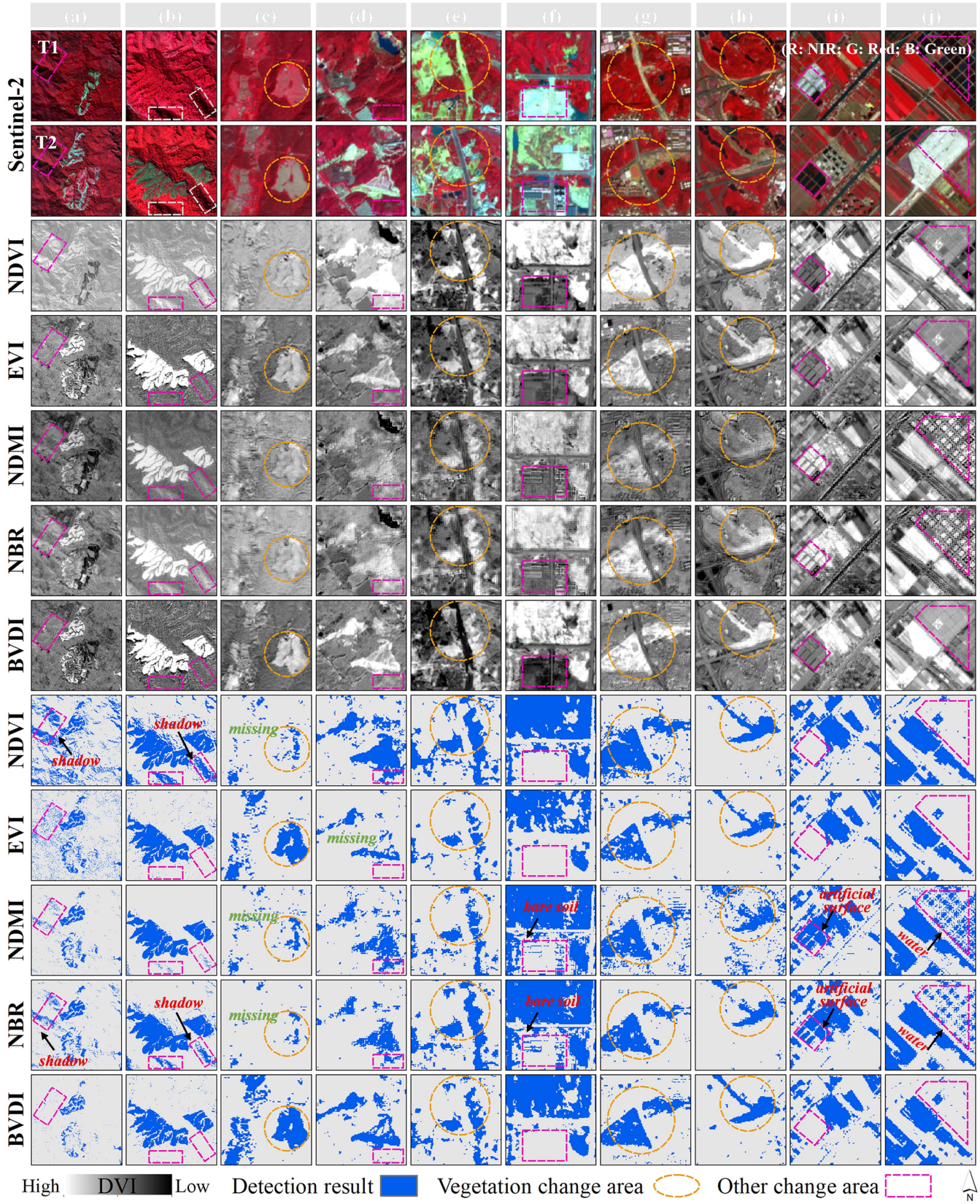

Fig. 10. Detection of vegetation changes in the context of changes in bare soil or man-made surfaces. (a) and (b) Topographic shadow changes. (c)–(f) Bare soil changes. (g)–(j) Artificial surface changes. The black and white plots represent visualization results of the index difference (i.e., DVI).

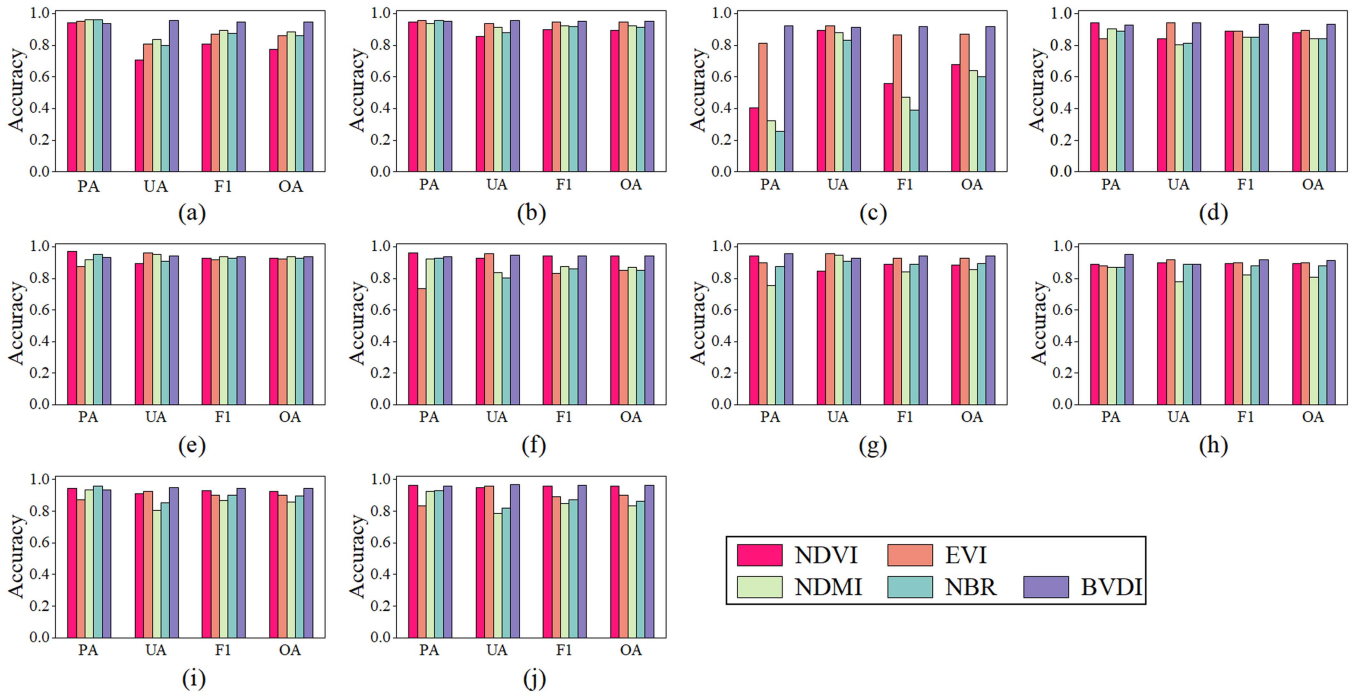

Fig. 11. Accuracy assessment of detection results of VIs in study sites (or Fig. 10) (a)–(j) a–j.

including water bodies, bare soil, and light conditions. The experiments confirmed that BVDI is feasible for various vegetation destruction events and has the best performance in excluding the interference of background change.

F. Visual Comparison With Related Products

Six wildfire events in Mediterranean countries were selected to visually compare the BVDI-based results with two data products. Note that the CEMS data in Fig. 15(e) and (f) is not shown because they are not available. For high-coverage vegetation areas, the BVDI-based results were highly consistent with the GLADFA and CEMS data [see Fig. 15(a), (e), and (f)]. However, for low-coverage vegetation areas, the results were significantly different [see Fig. 15(b)–(d)]. The CEMS data focused on the actual burned area and therefore also identified the burned area of nonphotosynthetic vegetation (including dry matter), thus overestimating the extent of vegetation destruction. This may be related to the purpose of the CEMS data. CEMS data is primarily used for postdisaster emergency management to assess more comprehensive disaster impacts. The GLADFA data omitted some vegetation change information, thus underestimating the extent of vegetation destruction [see Fig. 15(c) and (d)]. This may be caused by the low time-space resolution of the data used to develop GLADFA. The coarse spatial resolution may miss smaller patches of vegetation destruction, while the coarse temporal resolution fails to distinguish partial vegetation recovery after disasters. Overall, BVDI is an effective indicator for identifying vegetation changes, focusing on vegetation changes caused by various disasters.

V. Discussion

A. Cross-Sensor Applicability of BVDI

Frequency monitoring is essential for vegetation restoration and postdisaster management [63]. Combined use of Landsat and Sentinel imagery allows global observation every 2–3 days [10], [64]. To ensure the objectivity and reliability of the conclusions, two rules should be followed. First, two vegetation destruction cases were chosen to assess the cross-sensor applicability of BVDI. These cases include man-made urban construction (see Fig. S2) and natural wildfire events (see Fig. S3). Second, we tested all combinations of remote sensing data sources to assess the robustness of BVDI. When using a combination of Sentinel and Landsat data, we employed a nearest-neighbor method to resample Landsat imagery to 10 m. Based on our previous spectral analysis (see Section III-A), we observed consistent spectral trends in Landsat and Sentinel-2 imagery across several land cover types. This provides a theoretical basis for the application of BVDI to other sensors.

The DVI results and detection results using different image pairs are shown in Figs. S2 and S3. It is not difficult to see that DVI calculated using various image pairs effectively highlighted areas of vegetation destruction. In the urban construction scenario, the BVDI-based method achieved satisfactory results, with average PA, UA, F1, and OA values of 0.943, 0.952, 0.947, and 0.948, respectively (see Table SII). Similarly, for wildfire scenarios, the F1 and OA values of the BVDI-based method were greater than 0.90 (see Table SII). This study shows that satisfactory detection results were obtained using both Landsat and Sentinel-2 imagery. In general, it is competitive to detect vegetation destruction using BVDI on Landsat images. BVDI

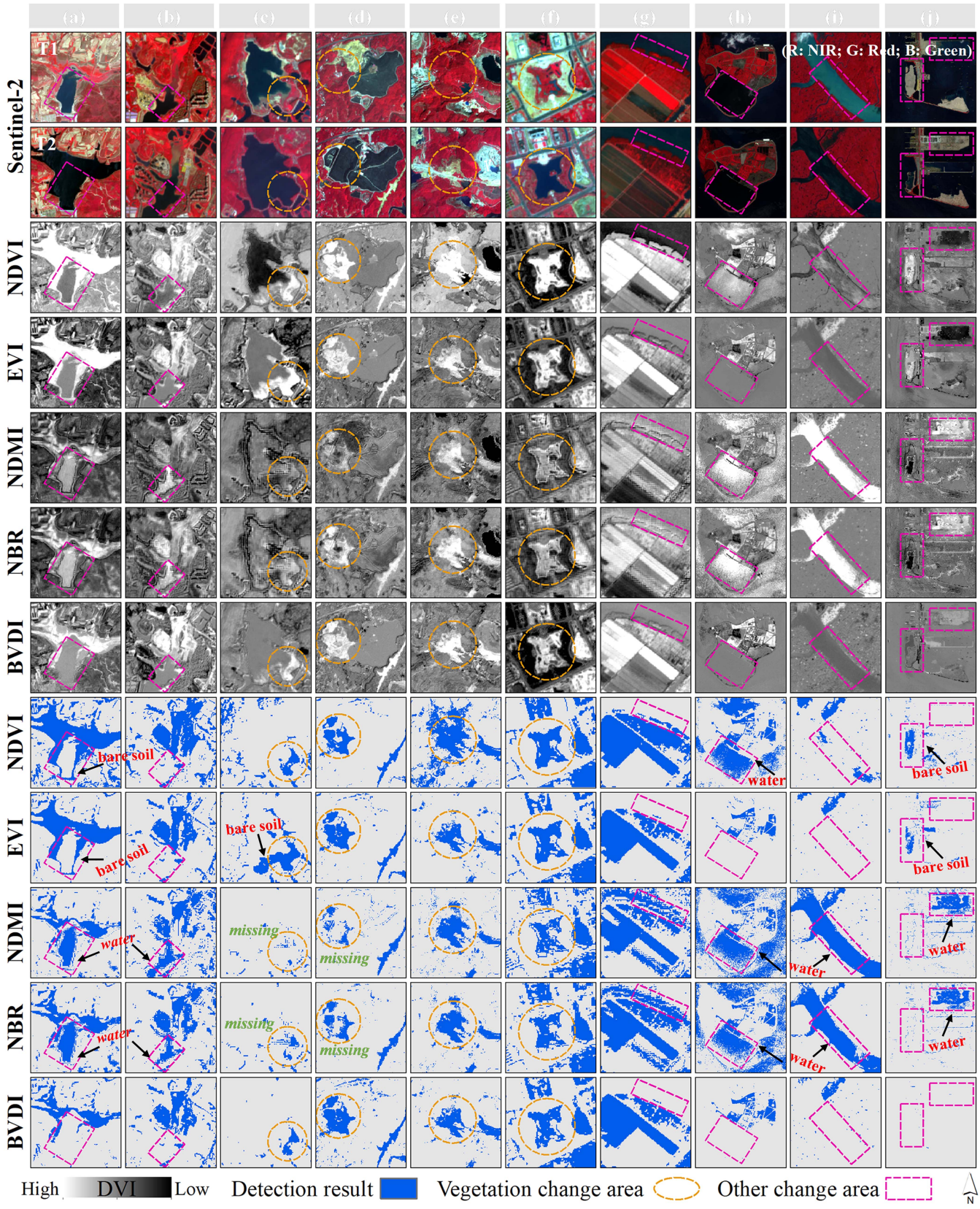

Fig. 12. Detection of vegetation changes in the context of water body changes. (a)–(d) Bare soil changes to water body. (e), (f), and (j) Water body changes to an artificial surface. (g)–(i) Water color changes. The black and white plots represent visualization results of the index difference (i.e., DVI).

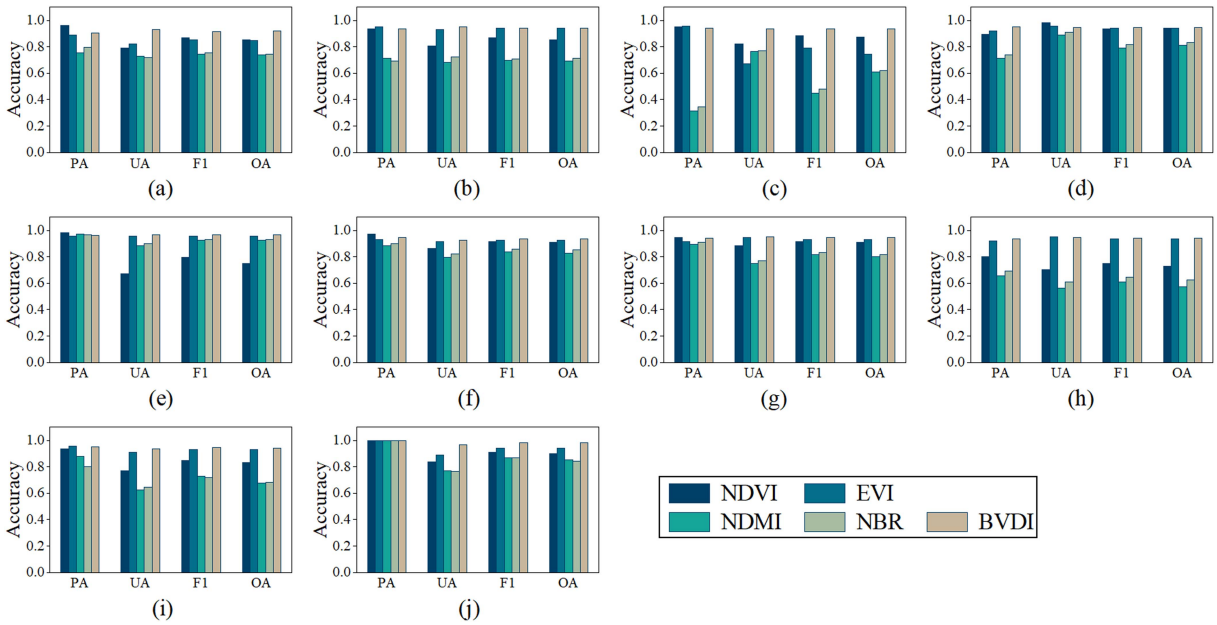

Fig. 13. Accuracy assessment of detection results of VIs in study site (or Fig. 12) (a)–(j) a–j.

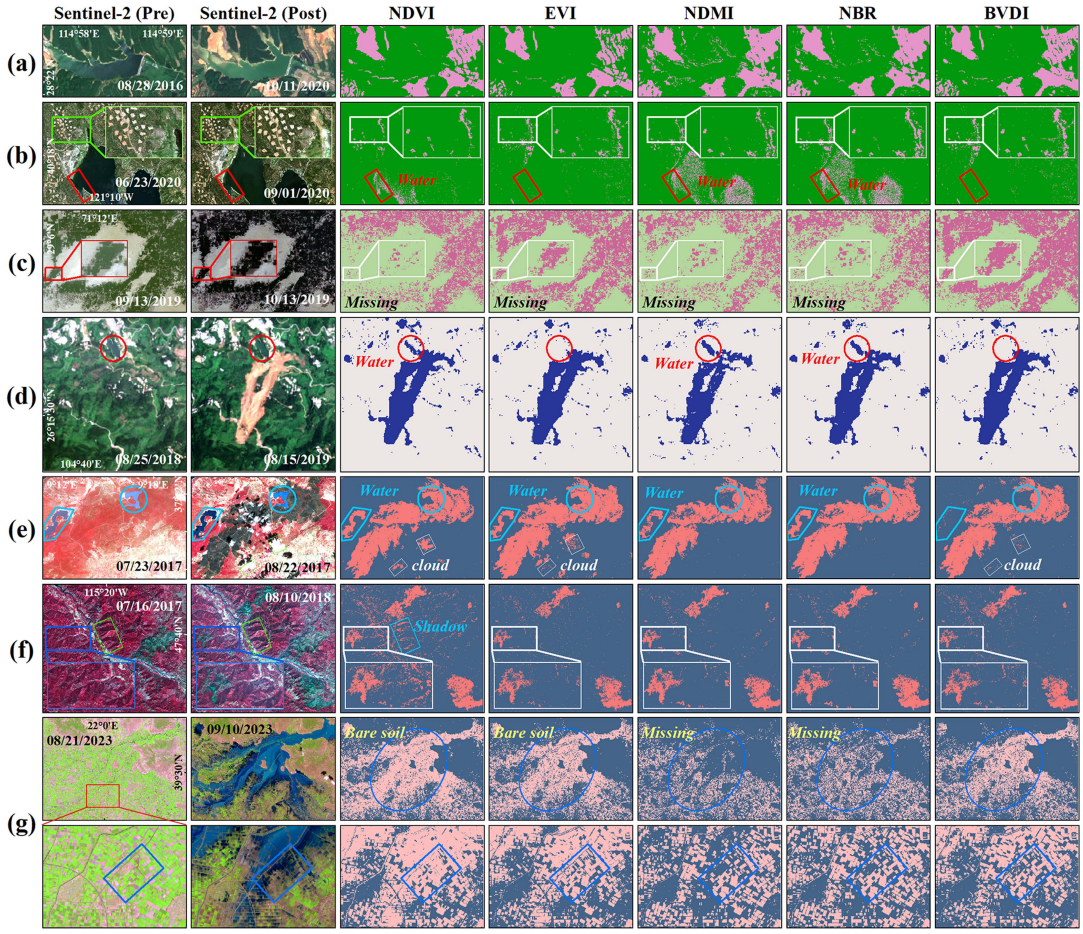

Fig. 14. Performance of VIs on vegetation destruction events. (a) Logging in Nanchang, China. (b) Logging in California, USA. (c) Locust infestation in Punjab, Pakistan. (d) Landslide in Guizhou, China. (e) Wildfire in Bizerte, Tunisia. (f) Wildfires in Montana, USA. (g) Floods in Magnesia, Greece.

TABLE II
DETECTION ACCURACY IN SEVERAL VEGETATION DESTRUCTION CASES

Number	Metric	a	b	c	d	e	f	g
NDVI-based	PA	0.963	0.923	0.757	0.940	0.913	0.940	0.953
	UA	0.881	0.769	0.887	0.890	0.690	0.718	0.862
	F1	0.920	0.839	0.817	0.914	0.786	0.814	0.905
	OA	0.917	0.823	0.830	0.912	0.752	0.785	0.900
EVI-based	PA	0.884	0.885	0.852	0.937	0.940	0.895	0.947
	UA	0.952	0.961	0.938	0.946	0.752	0.934	0.873
	F1	0.916	0.921	0.893	0.941	0.836	0.914	0.909
	OA	0.919	0.925	0.898	0.942	0.815	0.916	0.905
NDMI-based	PA	0.973	0.930	0.443	0.910	0.923	0.937	0.804
	UA	0.800	0.694	0.616	0.858	0.772	0.912	0.760
	F1	0.878	0.795	0.516	0.883	0.841	0.924	0.781
	OA	0.865	0.760	0.583	0.880	0.825	0.923	0.775
NBR-based	PA	0.970	0.917	0.490	0.897	0.920	0.943	0.855
	UA	0.827	0.671	0.615	0.862	0.784	0.931	0.820
	F1	0.893	0.775	0.546	0.879	0.857	0.937	0.837
	OA	0.883	0.733	0.592	0.877	0.833	0.937	0.834
BVDI-based	PA	0.947	0.942	0.947	0.960	0.916	0.932	0.936
	UA	0.931	0.936	0.931	0.957	0.927	0.925	0.940
	F1	0.939	0.939	0.939	0.959	0.922	0.929	0.938
	OA	0.938	0.939	0.938	0.958	0.922	0.928	0.939

exhibits robustness across various multispectral imagery as long as green, red, and NIR bands are available.

B. Advantages of BVDI

Accurate detection of vegetation damage events is crucial for ecological restoration [32], [33], [35]. Nevertheless, the application of existing spectral VIs on large scales remains challenging. Therefore, we proposed a novel index called (BVDI) by analyzing the spectral characteristics of various land covers and multiple vegetation destruction events. The experiments in Section IV proved that the BVDI-based method is effective in detecting vegetation change information in complex scenes, and exhibits robustness across multiple vegetation destruction events. The strengths of BVDI can be summarized in the following aspects.

First, BVDI makes full use of the three bands that exhibit the highest sensitivity to leaf biochemical content and canopy structure of vegetation, so it is highly sensitive to vegetation changes. Using the PROSAIL model, we analyzed the local sensitivity of spectra to changes in leaf biochemical content and canopy structure of vegetation (see Fig. 16). Vegetation displayed a small reflectance peak in the green band and a small absorption valley in the red band. With the increase of Cab, the reflectance of vegetation in the green band decreases while absorption in the red band increases. Moreover, vegetation exhibits a large reflection peak in the NIR band, and the reflection in the NIR band increases as the LAI of the vegetation increases. We found that the green and red bands are the two most sensitive to Cab, while the NIR band is highly sensitive to LAI. These observations align with prior research [44], [65]. Furthermore, BVDI consistently demonstrates a strong linear correlation with LAI at different Cab values, with R2 values of 0.97–0.98 (see Fig. 5). The results confirm that BVDI is sensitive to vegetation changes and does not exhibit a saturation effect. This is a crucial prerequisite for accurate detection of vegetation destruction.

Second, BVDI narrows differences between nonvegetation land cover and reduces the influence of background environmental changes. Mitigating the impact of background environmental changes is a critical challenge for accurately detecting vegetation changes. The "pseudo change" caused by the color change of water bodies and interconversion of water bodies and bare soil can easily be mistaken for "true change" in vegetation (see Fig. 12). NDVI, EVI, NDMI, and NBR were all susceptible to background environmental changes. Based on spectral analysis, it observed that in green, red, and NIR bands, vegetation exhibited a distinct

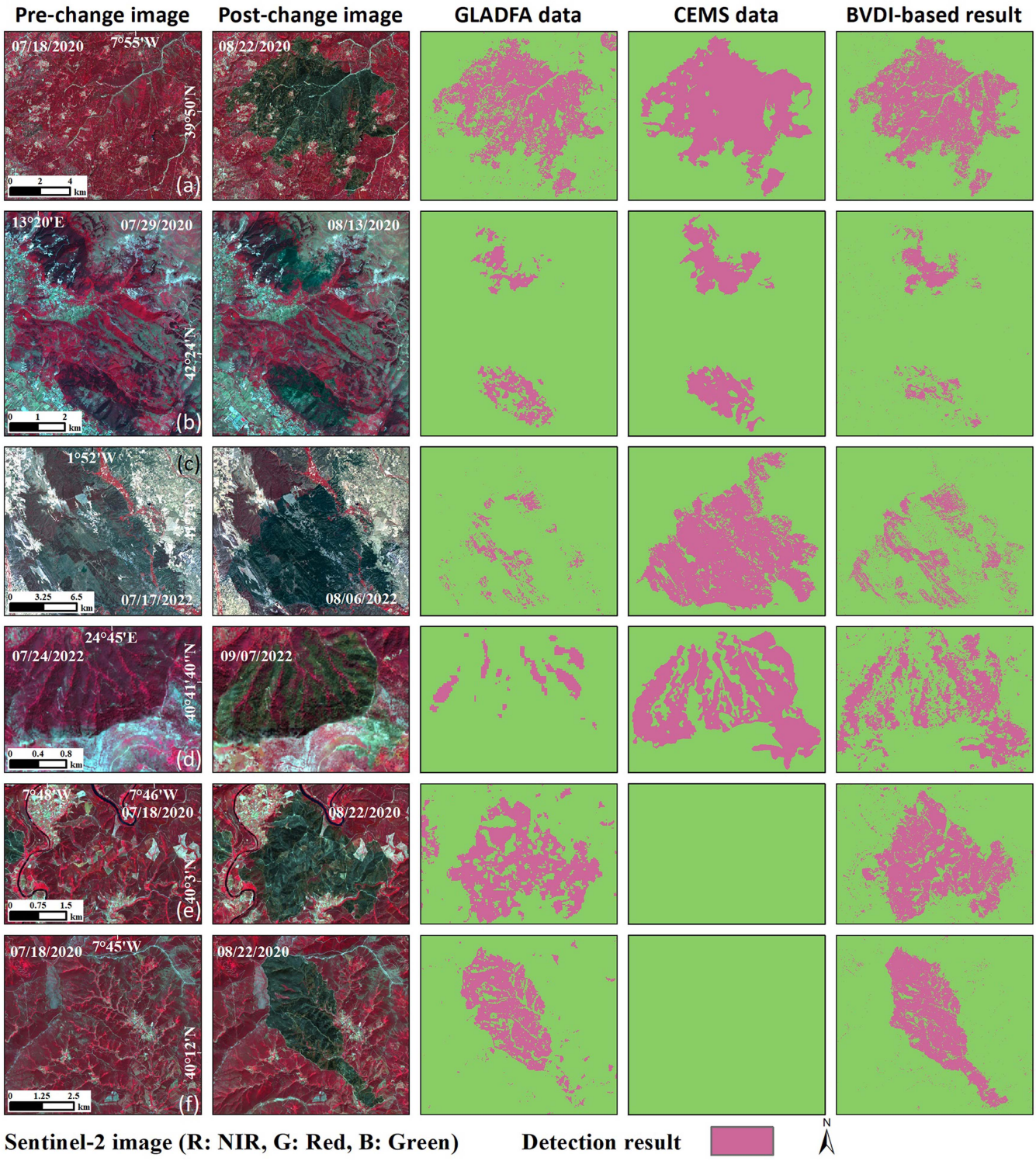

Fig. 15. Recognition results of GLADFA, CEMS, and BVDI-based method. (a) Portugal on July 25 2020. (b) Italy on July 25 2020. (c) Spain on July 18 2022. (d) Greece on August 10 2022. (e) Portugal on July 20 2020. (f) Portugal on August 6 2020.

"V-shaped valley" characteristic, while nonvegetation land covers and vegetation destruction events displayed a "near-linear" trend (see Figs. 3 and 4). Using this principle, we proposed BVDI. In the BVDI image, vegetation exhibits high values, while nonvegetation land covers and vegetation destruction events cluster around the 0 value. Through the experiments in Section IV, we proved that the BVDI has significant advantages when the background environmental changes.

Third, BVDI is an effective indicator for multispectral sensors such as Sentinel-2 and Landsat. The synergistic use of

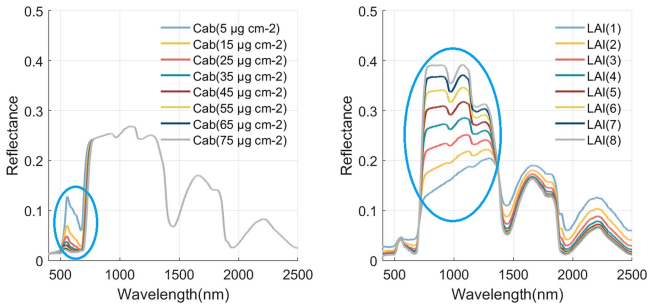

Fig. 16. Simulation of spectral profiles with different Cab and LAI using the PROSAIL model.

multiple sensors is of great value for vegetation monitoring at high frequency. We found that several typical land covers showed consistent spectral trends in Landsat and Sentinel-2 imagery (see Fig. S1). BVDI proved to be a reliable indicator of vegetation destruction detection in Landsat-8, Landsat-9, and Sentinel-2 imagery (see Fig. 7). We demonstrated this advantage using the man-made urban construction cases and natural wildfire events (see Figs. S2 and S3). Landsat-8, Landsat-9, and Sentinel-2 are the most commonly used satellite sensors that provide systematic global land surface observations [41], [64]. Overall, BVDI can be effectively used for vegetation monitoring in different global regions, offering great promise for large-scale and high-frequency vegetation destruction detection.

C. Limitations of This Workflow and Future Improvements

Despite the above advantages, this study has some limitations and possible improvements. First, BVDI was developed utilizing bands sensitive to vegetation leaves and canopy, characterized by shorter wavelengths that are susceptible to the influence of thin clouds and cloud shadows [see Fig. 14(e)]. Previous studies have indicated that the SWIR band exhibits more sensitivity to vegetation water content, offering valuable information for vegetation change monitoring [24], [66], [67], [68]. Moreover, considering the longer wavelength of the SWIR band, which reduces the effect of cloud cover, its incorporation will be contemplated in future enhancements. Second, due to the absence of available field investigation data, instances of vegetation infestations involving pests like the spruce beetle and birch moth were not encompassed in this study. Some studies [67], [69], [70] have reported the substantial harm inflicted by these pests on vegetation ecosystems. Further exploration is required to assess BVDI's performance in these scenarios. Third, the image difference method may recognize field operations as vegetation destruction. To address this, additional prior knowledge is essential for eliminating such interference, which may involve utilizing historical contemporaneous images [8], [41]. In the future, we will also explore the ability of BVDI for real-time vegetation monitoring using time-series data.

VI. Conclusion

In this study, we proposed a baseline-based vegetation destruction index (named BVDI) using the red, green, and NIR bands of Sentinel-2 imagery to achieve accurate detection of multiple vegetation destruction events. We assessed the effectiveness of BVDI through the dual-temporal image difference method and conducted a detailed comparison with four classical VIs. Using the simulation data of the PROSAIL model, we found that BVDI exhibited a strong linear correlation with LAI under different chlorophyll contents. BVDI demonstrated effectiveness and robustness in various vegetation change scenarios, especially underwater changes, which was better than the existing VIs. Experiments on loggings, insect infestations, landslides, wildfires, and floods further proved the robustness of BVDI, with OA values of 0.923–0.963 and F1 scores of 0.924–0.963. To conclude, BVDI is a robust spectral metric suitable for various vegetation destruction events, with significant advantages under complex background environmental changes. We believe that this study is valuable for regional and even global vegetation monitoring and diagnosis.

References

[1] M. Zhou, D. Li, K. Liao, and D. Lu, "Integration of Landsat time-series vegetation indices improves consistency of change detection," *Int. J. Digit. Earth*, vol. 16, no. 1, pp. 1276–1299, 2023.
[2] S. L. Middleton, "Automating image segmentation for vegetation monitoring," *Nature Rev. Earth Environ.*, vol. 4, 2023, Art. no. 807.
[3] Y. Liu, H. Liu, Y. Chen, C. Gang, and Y. Shen, "Quantifying the contributions of climate change and human activities to vegetation dynamic in China based on multiple indices," *Sci. Total Environ.*, vol. 838, pp. 156553–156563, 2022.
[4] Y. Wei, H. Lu, J. Wang, X. Wang, and J. Sun, "Dual influence of climate change and anthropogenic activities on the spatiotemporal vegetation dynamics over the Qinghai-Tibetan Plateau from 1981 to 2015," *Earth's Future*, vol. 10, no. 5, pp. 2566–2588, 2022.
[5] S. Sannigrahi et al., "Examining the effects of forest fire on terrestrial carbon emission and ecosystem production in India using remote sensing approaches," *Sci. Total Environ.*, vol. 725, pp. 138331–138343, 2020.
[6] Y. Zhang et al., "Mapping causal agents of disturbance in boreal and arctic ecosystems of North America using time series of Landsat data," *Remote Sens. Environ.*, vol. 272, pp. 112935–112942, Apr. 2022.
[7] E. J. Bowd, S. C. Banks, C. L. Strong, and D. B. Lindenmayer, "Long-term impacts of wildfire and logging on forest soils," *Nature Geosci.*, vol. 12, no. 2, pp. 113–118, 2019.
[8] C. Zhao et al., "Monitoring of deforestation events in the tropics using multidimensional features of Sentinel 1 radar data," *Front. Forests Glob. Change*, vol. 6, pp. 1257806–1257823, 2023.
[9] E. Veldkamp, M. Schmidt, J. S. Powers, and M. D. Corre, "Deforestation and reforestation impacts on soils in the tropics," *Nature Rev. Earth Environ.*, vol. 1, no. 11, pp. 590–605, 2020.
[10] X.-P. Song et al., "Global land change from 1982 to 2016," *Nature*, vol. 560, no. 7720, pp. 639–643, 2018.
[11] S. I. Higgins, T. Conradi, and E. Muhoko, "Shifts in vegetation activity of terrestrial ecosystems attributable to climate trends," *Nature Geosci.*, vol. 16, no. 2, pp. 147–153, 2023.
[12] M. Wei, Z. Zhang, T. Long, G. He, and G. Wang, "Monitoring landsat based burned area as an indicator of sustainable development goals," *Earths Future*, vol. 9, no. 6, pp. 1960–1975, 2021.
[13] C. Y. Park et al., "How will deforestation and vegetation degradation affect global fire activity?," *Earth's Future*, vol. 9, no. 5, 2021, Art. no. e2020EF001786.
[14] A. M. Lechner, G. M. Foody, and D. S. Boyd, "Applications in remote sensing to forest ecology and management," *One Earth*, vol. 2, no. 5, pp. 405–412, 2020.
[15] A. Shama et al., "A burned area extracting method using polarization and texture feature of Sentinel-1a images," *IEEE Geosci. Remote Sens. Lett.*, vol. 20, 2023, Art. no. 2501305.
[16] D. P. Roy, L. Boschetti, and S. N. Trigg, "Remote sensing of fire severity: Assessing the performance of the normalized burn ratio," *IEEE Geosci. Remote Sens. Lett.*, vol. 3, no. 1, pp. 112–116, Jan. 2006.

[17] W. Guo, C. Zhao, Y. Zhang, and S. Gao, "Mapping impervious surface distribution and dynamics in an arid/semiarid area-a case study in Ordos, China," *IEEE Access*, vol. 9, pp. 19659–19673, 2021.

[18] D. L. A. Gaveau, A. Descals, M. A. Salim, D. Sheil, and S. Sloan, "Refined burned-area mapping protocol using Sentinel-2 data increases estimate of 2019 Indonesian burning," *Earth Syst. Sci. Data*, vol. 13, no. 11, pp. 5353–5368, 2021.

[19] A. Radman, R. Shah-Hosseini, and S. Homayouni, "A deep convolutional neural network for burn progression mapping using Sentinel-1 SAR time-series," *Int. J. Remote Sens.*, vol. 44, no. 7, pp. 2196–2215, Apr. 2023.

[20] A. Y. Cho, S.-E. Park, D.-J. Kim, J. Kim, C. Li, and J. Song, "Burned area mapping using unitemporal planetscope imagery with a deep learning based approach," *IEEE J. Sel. Topics Appl. Earth Observ. Remote Sens.*, vol. 16, pp. 242–253, 2023.

[21] Y. Cao et al., "Forest disaster detection method based on ensemble spatial–spectral genetic algorithm," *IEEE J. Sel. Topics Appl. Earth Observ. Remote Sens.*, vol. 15, pp. 7375–7390, 2022.

[22] F. Ji et al., "Coupling physical model and deep learning for near real-time wildfire detection," *IEEE Geosci. Remote Sens. Lett.*, vol. 20, 2023, Art. no. 6009205.

[23] P. K. Das, A. Sahu, D. V. Xavy, and S. Meher, "A deforestation detection network using deep learning-based semantic segmentation," *IEEE Sens. Lett.*, vol. 8, no. 1, Jan. 2024, Art. no. 7000104.

[24] S. Liu, Y. Zheng, M. Dalponte, and X. Tong, "A novel fire index-based burned area change detection approach using Landsat-8 OLI data," *Eur. J. Remote Sens.*, vol. 53, no. 1, pp. 104–112, 2020.

[25] H. Abdullah, A. K. Skidmore, R. Darvishzadeh, and M. Heurich, "Timing of red-edge and shortwave infrared reflectance critical for early stress detection induced by bark beetle (Ips typographus, L.) attack," *Int. J. Appl. Earth Observ. Geoinf.*, vol. 82, pp. 101900–101912, Oct. 2019.

[26] J. Peereman, J. Aaron Hogan, and T.-C. Lin, "Intraseasonal interactive effects of successive typhoons characterize canopy damage of forests in Taiwan: A remote sensing-based assessment," *Forest Ecol. Manage.*, vol. 521, pp. 120430–120441, 2022.

[27] J. H. Lee, "Prediction of large-scale wildfires with the canopy stress index derived from soil moisture active passive," *IEEE J. Sel. Topics Appl. Earth Observ. Remote Sens.*, vol. 14, pp. 2096–2102, 2021.

[28] E. Alcaras, D. Costantino, F. Guastaferro, C. Parente, and M. Pepe, "Normalized burn ratio plus (NBR plus): A new index for Sentinel-2 imagery," *Remote Sens*, vol. 14, no. 7, Apr. 2022, Art. no. 1727.

[29] N. Afira and A. W. Wijayanto, "Mono-temporal and multi-temporal approaches for burnt area detection using Sentinel-2 satellite imagery (a case study of Rokan Hilir Regency, Indonesia)," *Ecol. Inform.*, vol. 69, pp. 101677–101695, 2022.

[30] J. Peereman, J. A. Hogan, and T. C. Lin, "Disturbance frequency, intensity and forest structure modulate cyclone-induced changes in mangrove forest canopy cover," *Glob. Ecol. Biogeogr.*, vol. 31, no. 1, pp. 37–50, 2021.

[31] H. R. Pourghasemi, S. Pouyan, M. Bordbar, F. Golkar, and J. J. Clague, "Flood, landslides, forest fire, and earthquake susceptibility maps using machine learning techniques and their combination," *Nature Hazards*, vol. 116, no. 3, pp. 3797–3816, Feb. 2023.

[32] B. Adamu, K. Tansey, and B. Ogutu, "Remote sensing for detection and monitoring of vegetation affected by oil spills," *Int. J. Remote Sens.*, vol. 39, no. 11, pp. 3628–3645, 2018.

[33] Y. Xu et al., "Automatically identifying the vegetation destruction and restoration of various open-pit mines utilizing remotely sensed images: Auto-VDR," *J. Cleaner Prod.*, vol. 414, 2023, Art. no. 137490.

[34] S. T. Seydi, M. Hasanlou, and J. Chanussot, "A quadratic morphological deep neural network fusing radar and optical data for the mapping of burned areas," *IEEE J. Sel. Topics Appl. Earth Observ. Remote Sens.*, vol. 15, pp. 4194–4216, 2022.

[35] Y. Yang, P. Erskine, A. Lechner, D. Mulligan, S. Zhang, and Z. Wang, "Detecting the dynamics of vegetation disturbance and recovery in surface mining area via Landsat imagery and LandTrendr algorithm," *J. Cleaner Prod.*, vol. 178, pp. 353–362, Mar. 2018.

[36] H. Li, B. Zhou, and F. Xu, "Variation analysis of spectral characteristics of reclamation vegetation in a rare earth mining area under environmental stress," *IEEE Trans. Geosci. Remote Sens.*, vol. 60, 2022, Art. no. 4408412.

[37] C. C. Pérez, A. E. Olthoff, H. Hernández-Trejo, and C. D. Rullán-Silva, "Evaluating the best spectral indices for burned areas in the tropical Pantanos de Centla Biosphere Reserve, southeastern Mexico," *Remote Sens. Appl.-Soc. Environ.*, vol. 25, pp. 100664–100677, 2022.

[38] S. König, F. Thonfeld, M. Förster, O. Dubovyk, and M. Heurich, "Assessing combinations of landsat, Sentinel-2 and Sentinel-1 time series for detecting bark beetle infestations," *GISci. Remote Sens.*, vol. 60, no. 1, 2023, Art. no. 2226515.

[39] Y. Wang et al., "Vegetation disturbances characterization in the Tibetan Plateau from 1986 to 2018 using Landsat time series and field observations," *Environ. Res. Lett.*, vol. 18, no. 1, pp. 014016–014029, 2023.

[40] M. S. Rahman, L. Di, E. Yu, L. Lin, and Z. Yu, "Remote sensing based rapid assessment of flood crop damage using novel disaster vegetation damage index (DVDI)," *Int. J. Disaster Risk Sci.*, vol. 12, no. 1, pp. 90–110, 2020.

[41] Z. Qi, A. Gar-On Yeh, X. Li, and X. Liu, "A land clearing index for high-frequency unsupervised monitoring of land development using multi-source optical remote sensing images," *ISPRS J. Photogrammetry Remote Sens.*, vol. 187, pp. 393–421, 2022.

[42] A. M. Baldridge, S. J. Hook, C. I. Grove, and G. Rivera, "The ASTER spectral library version 2.0," *Remote Sens. Environ.*, vol. 113, no. 4, pp. 711–715, 2009.

[43] Y. Liu, Q. Meng, L. Zhang, and C. Wu, "NDBSI: A normalized difference bare soil index for remote sensing to improve bare soil mapping accuracy in urban and rural areas," *Catena*, vol. 214, pp. 106265–106274, 2022.

[44] S. Jacquemoud et al., "PROSPECT+SAIL models: A review of use for vegetation characterization," *Remote Sens. Environ.*, vol. 113, pp. S56–S66, 2009.

[45] K. Berger et al., "Evaluation of the PROSAIL model capabilities for future hyperspectral model environments: A review study," *Remote Sens*, vol. 10, no. 2, pp. 85–110, 2018.

[46] D. Li et al., "Assessing a soil-removed semi-empirical model for estimating leaf chlorophyll content," *Remote Sens. Environ.*, vol. 282, pp. 113284–113300, 2022.

[47] W. Li et al., "RSARE: A physically-based vegetation index for estimating wheat green LAI to mitigate the impact of leaf chlorophyll content and residue-soil background," *ISPRS J. Photogrammetry Remote Sens.*, vol. 200, pp. 138–152, 2023.

[48] Z. Wang et al., "Generality of leaf spectroscopic models for predicting key foliar functional traits across continents: A comparison between physically- and empirically-based approaches," *Remote Sens. Environ.*, vol. 293, pp. 113614–113630, 2023.

[49] L. Wan et al., "PROSDM: Applicability of PROSPECT model coupled with spectral derivatives and similarity metrics to retrieve leaf biochemical traits from bidirectional reflectance," *Remote Sens. Environ.*, vol. 267, pp. 112761–112778, 2021.

[50] L. Spafford, G. le Maire, A. MacDougall, F. de Boissieu, and J.-B. Féret, "Spectral subdomains and prior estimation of leaf structure improves PROSPECT inversion on reflectance or transmittance alone," *Remote Sens. Environ.*, vol. 252, pp. 112176–112191, 2021.

[51] V. Fotakidis, I. Chrysafis, G. Mallinis, and N. Koutsias, "Continuous burned area monitoring using bi-temporal spectral index time series analysis," *Int. J. Appl. Earth Observ. Geoinf.*, vol. 125, 2023, Art. no. 103547.

[52] L. Liang et al., "Estimation of crop LAI using hyperspectral vegetation indices and a hybrid inversion method," *Remote Sens. Environ.*, vol. 165, pp. 123–134, 2015.

[53] M. Schultz et al., "Performance of vegetation indices from Landsat time series in deforestation monitoring," *Int. J. Appl. Earth Observ. Geoinf.*, vol. 52, pp. 318–327, 2016.

[54] Y. Zeng et al., "Optical vegetation indices for monitoring terrestrial ecosystems globally," *Nature Rev. Earth Environ.*, vol. 3, no. 7, pp. 477–493, Jul. 2022.

[55] M. Decuyper et al., "Continuous monitoring of forest change dynamics with satellite time series," *Remote Sens. Environ.*, vol. 269, 2022, Art. no. 112829.

[56] Y. Zhang, S. Liu, Y. Wang, H. Gao, Y. Jiang, and D. Wei, "Forest management practices and policies exert strong impacts on the spatio-temporal variations of forest disturbance in Hunan Province, China over the last three decades," *Forest Ecol. Manage.*, vol. 544, 2023, Art. no. 121167.

[57] H. Fang, S. Guo, X. Wang, S. Liu, C. Lin, and P. Du, "Automatic urban scene-level binary change detection based on a novel sample selection approach and advanced triplet neural network," *IEEE Trans. Geosci. Remote Sens.*, vol. 61, 2023, Art. no. 5601518.

[58] H. Fang, P. Du, and X. Wang, "A novel unsupervised binary change detection method for VHR optical remote sensing imagery over urban areas," *Int. J. Appl. Earth Observ. Geoinf.*, vol. 108, pp. 102749–102761, 2022.

[59] M.-T. Pham, G. Mercier, and J. Michel, "Change detection between SAR images using a pointwise approach and graph theory," *IEEE Trans. Geosci. Remote Sens.*, vol. 54, no. 4, pp. 2020–2032, Apr. 2016.

[60] C. Zhao and Y. Pan, "A novel spectral index for mapping blue colour-coated steel roofs (BCCSRs) in urban areas using Sentinel-2 data," *Int. J. Digit. Earth*, vol. 16, no. 1, pp. 2862–2884, 2023.

[61] P. Zhang et al., "A novel index for robust and large-scale mapping of plastic greenhouse from Sentinel-2 images," *Remote Sens. Environ.*, vol. 276, pp. 113042–113063, 2022.
[62] B. DeVries, M. Decuyper, J. Verbesselt, A. Zeileis, M. Herold, and S. Joseph, "Tracking disturbance-regrowth dynamics in tropical forests using structural change detection and Landsat time series," *Remote Sens. Environ.*, vol. 169, pp. 320–334, 2015.
[63] T. Ma, T. Wang, D. Yang, and S. Yang, "Impacts of vegetation restoration on water resources and carbon sequestration in the mountainous area of Haihe River basin, China," *Sci. Total Environ.*, vol. 869, 2023, Art. no. 161724.
[64] N. Chen, N.-E. Tsendbazar, E. Hamunyela, J. Verbesselt, and M. Herold, "Sub-annual tropical forest disturbance monitoring using harmonized Landsat and Sentinel-2 data," *Int. J. Appl. Earth Observ. Geoinf.*, vol. 102, pp. 102386–102397, 2021.
[65] J. Liu, J. Fan, C. Yang, F. Xu, and X. Zhang, "Novel vegetation indices for estimating photosynthetic and non-photosynthetic fractional vegetation cover from Sentinel data," *Int. J. Appl. Earth Observ. Geoinf.*, vol. 109, pp. 102793–102804, 2022.
[66] M. J. van Gerrevink and S. Veraverbeke, "Evaluating the hyperspectral sensitivity of the differenced normalized burn ratio for assessing fire severity," *Remote Sens.*, vol. 13, no. 22, pp. 4611–4626, 2021.
[67] L. Huo, H. J. Persson, and E. Lindberg, "Early detection of forest stress from European spruce bark beetle attack, and a new vegetation index: Normalized distance red & SWIR (NDRS)," *Remote Sens. Environ.*, vol. 255, pp. 112240–112257, 2021.
[68] J. Tian and W. D. Philpot, "Relationship between surface soil water content, evaporation rate, and water absorption band depths in SWIR reflectance spectra," *Remote Sens. Environ.*, vol. 169, pp. 280–289, 2015.
[69] J. U. Jepsen, O. P. L. Vindstad, and R. A. Ims, "Spatiotemporal dynamics of forest geometrid outbreaks," *Curr. Opin. Insect Sci.*, vol. 55, pp. 100990–100997, 2023.
[70] A. Safonova, Y. Hamad, A. Alekhina, and D. Kaplun, "Detection of Norway spruce trees (picea abies) infested by bark beetle in UAV images using YOLOs architectures," *IEEE Access*, vol. 10, pp. 10384–10392, 2022.

Chuanwu Zhao (Graduate Student Member, IEEE) was born in Xinyang, Henan, China, in 1995. He is currently working toward the Ph.D. degree in cartography and geographic information system with the State Key Laboratory of Remote Sensing Science, Faculty of Geographical Science, Beijing Normal University, Beijing, China.

His research interests include remote-sensing image processing, urban remote sensing, and vegetation anomaly detection.

Yaozhong Pan received the B.S. degree in remote sensing technology from Zhejiang University, Hangzhou, China, in 1988, and the M.S. and Ph.D. degrees in physical geography from Beijing Normal University, Beijing, China, in 1994 and 1997, respectively.

He is currently a Professor with Beijing Normal University, where he is currently the Dean with the Institute of Remote Sensing Science and Engineering. He has authored or coauthored more than 150 peer-reviewed international journal articles. His research interests include agricultural intelligent remote sensing and real-time remote sensing of surface anomalies.

Dr. Pan was the recipient of several research awards, including the first prize in the Mapping Science and Technology Progress Award in 2015 and 2017, and the first prize in the Beijing Science and Technology Award in 2018.

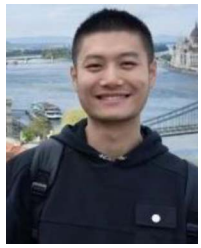

Hanyi Wu (Graduate Student Member, IEEE) received the B.S. degree in remote sensing science and technology from Nanjing University of Information Science and Technology, Nanjing, China, in 2022, and he is currently working toward the M.S. degree in cartography and geographic information system with the State Key Laboratory of Remote Sensing Science, Faculty of Geographical Science, Beijing Normal University, Beijing, China.

His research interests include remote-sensing image processing, urban remote sensing, health risk assessment, and agricultural intelligent remote sensing.

Shoujia Ren (Graduate Student Member, IEEE) was born in Qingdao, Shandong, China, in 1996. He is currently working toward the Ph.D. degree in cartography and geographic information system with the State Key Laboratory of Remote Sensing Science, Faculty of Geographical Science, Beijing Normal University, Beijing, China.

His research interests include remote-sensing image processing, urban remote sensing, and artificial surface anomaly detection.

Gelilan Ma was born in Hengyang, Hunan, China, in 2001. She received the B.S. degree in natural geography and resources environment from Beijing Forestry University, Beijing, China, in 2023. She is currently working toward the M.S. degree in cartography and geographic information system with the State Key Laboratory of with the State Key Laboratory of Remote Sensing Science, Faculty of Geographical Science, Beijing Normal University, Beijing, China.

Her research interests include remote-sensing image processing and water anomaly detection.

Yuan Gao (Graduate Student Member, IEEE) was born in Shuozhou, Shanxi, China, in 1996. She is currently working toward the Ph.D. degree in cartography and geographic information system with the State Key Laboratory of Remote Sensing Science, Faculty of Geographical Science, Beijing Normal University, Beijing, China.

Her research interests include remote-sensing image processing, agricultural remote sensing, and land cover mapping.

Yu Zhu was born in Quzhou, Zhejiang, China, in 1998. He is currently working toward the Ph.D. degree in remote sensing science and technology with the State Key Laboratory of Remote Sensing Science, Faculty of Geographical Science, Beijing Normal University, Beijing, China.

His research interests include deep learning-based image processing and agricultural intelligent remote sensing.

Guifei Jing received the B.S. and M.S. degrees in geography from Peking University, Beijing, China, in 1991 and 1994, respectively, and the Ph.D. degree in geography from Beijing Normal University, Beijing, China, in 2004.

He is currently a Researcher with the Research Institute for Frontier Science, Beihang University. His main research interests include remote sensing applications, information acquisition, and processing technologies.